MSc Thesis Title

by

Shabnam Fadaei Chatroudi

A Dissertation Submitted to the
Graduate School of Sciences and Engineering
in Partial Fulfillment of the Requirements for
the Degree of

Master of Science

in

Materials Science and Engineering

KOÇ
ÜNİVERSİTESİ

January , 2022

A Numerical and Experimental Design of High Entropy Alloys for Biomedical Applications

Koç University

Graduate School of Sciences and Engineering

This is to certify that I have examined this copy of a master's thesis by

Shabnam Fadaei Chatroudi

and have found that it is complete and satisfactory in all respects,
and that any and all revisions required by the final
examining committee have been made.

Committee Members:

_____

Professor Demircan Canadinç (Advisor)

_____

Associate Professor Ozan Kocadağlı

_____

Assistant Professor S. Mine Toker

Date: 3/1/2022

Dedicated to my family.

ABSTRACT

A Numerical and Experimental Design of High Entropy Alloys for Biomedical Applications

Shabnam Fadaei Chatroudi

Master of Science in Materials Science and Engineering

January 2021

High entropy alloys are a relatively new type of multi-component alloys that attracted researcher's attention because of their superior properties, which mainly come from their high mixing entropy. Some of their main features are excellent mechanical and corrosion properties that lead them to be a potential candidate for biomedical applications. In this study, both numerical and experimental methods were used to enhance the biocompatibility of high entropy alloys. A machine learning approach was implemented to design a high entropy alloy with desired properties. Two unsupervised machine learning clustering techniques were performed to design a high entropy alloy with excellent biocompatibility properties. The characteristics required for these alloys to be used in biomedical applications were used as the input dataset of the models. These features were mainly pure metal's physical, chemical, mechanical, and biocompatibility properties, such as elastic modulus or cell viability measurements. Furthermore, a magnetron sputtering method was utilized to coat the high entropy alloys with silver for introducing antibacterial properties. The parameters of experiments were adjusted to achieve a coating film with desirable characteristics. It was shown that by increasing the deposition duration, the coating thickness and grain size increased, which can enhance the antibacterial characteristics. The ion release of coated samples was then measured after immersing in simulated body fluid for fourteen days. The measurements demonstrated that the Ag ion release increased by increasing the coating thickness, but the ion release of substrate elements stayed almost the same. Consequently, the higher release of Ag ions may lead to a better antibacterial effect since it is the main factor controlling antibacterial characteristics.

ÖZETÇE

Yüksek Lisans Tez Başlığı

Shabnam Fadaei Chatroudi

Malzeme Bilimleri ve Mühendisliği, Yüksek Lisans

Ocak 2021

Yeni bir tür çok bileşenli alaşım olan yüksek entropili alaşımlar sahip oldukları yüksek karışım entropisinden kaynaklanan üst düzey özelliklerden dolayı birçok araştırmacının ilgisini çekmiştir. Üstün mekanik ve korozyon özellikleri bu alaşımları biyomedikal uygulamalar için potansiyel aday yapan ana özelliklerden bazılarıdır. Bu çalışmada, yüksek entropili alaşımların biyouyumluluğunu geliştirmek için hem hesaplamalı hem de deneysel yöntemler uygulanmıştır. İstenilen özelliklere sahip bir yüksek entropili alaşım tasarlamak için makine öğrenmesi tekniği uygulanmıştır. Çok iyi biyouyumluluk özelliklerine sahip bir yüksek entropili alaşım tasarlamak için iki farklı gözetimsiz makine öğrenmesi tekniği kullanılmıştır. Bu alaşımların biyomedikal uygulamalarda kullanılabilmesi için gerekli olan karakteristik özellikler modeller için girdi olarak kullanılmıştır. Bu özellikler özellikle saf metallerin fiziksel, kimyasal, ve mekanik özellikleri olan sertlik ve hücre canlılık ölçümleridir. Ayrıca, yüksek entropili alaşımların anti bakteriyel özelliklerini geliştirmek için bu alaşımlar magnetron püskürtme yöntemi kullanılarak gümüş ile kaplanmıştır. İstenilen özelliklere sahip kaplamayı elde edebilmek için bazı deneysel parametreler değiştirilmiştir. Kaplama süresi uzatılarak, kaplamanın kalınlığı ve tanecik boyutunun artmasının anti bakteriyel özellikleri arttıracağı gösterilmiştir. Sonrasında, yapay kanda ön dört günlük süre sonunda kaplamaların iyon salınım miktarları ölçülmüştür. Ölçümler gümüş iyon salınımının kaplama kalınlığı ile arttığını ancak substrat elementlerinin salınımının değişmediğini göstermiştir. Son olarak, salınan gümüş iyonları ile anti bakteriyel süreç arasındaki doğrusal ilişki göz önünde bulundurulduğunda yüksek gümüş iyon salınımı daha iyi bir anti bakteriyel etkiye sebebiyet verebilir.

ACKNOWLEDGMENTS

First of all, I would like to express my special thanks to my advisor Prof. Demircan Canadinc who gave me this excellent opportunity to join his elite research group. His guidance, support, motivation, and knowledge helped me to overcome the obstacles throughout my way and made it possible to accomplish my study goals. Besides my advisor, I would also like to especially thank the rest of my thesis committee members Dr. Ozan Kocadağlı and Dr. Mine Toker, for their insights, time, and participation.

I would also show my gratitude to Dr. Baris Yagci that performed and guided me through most of my analyses during my study. It was a pleasure to be a member of the AMG group as they were like a family to me. I thank all of my fellow lab-mates, especially Huseyin Can Ozdemir and Alireza Nazarahari, who supported me through all my study with their friendship, companionship, and knowledge besides Ibrahim Burkay Tugluca Aysel Aysu Catal and Azize Hosseinjany and also my dear friend Ezgi Demiroz.

TABLE OF CONTENTS

LIST OF TABLES

LIST OF FIGURES

ABBREVIATIONS

MPEA	Multi Principal Element Alloys
HEA	High Entropy Alloy
AI	Artificial Intelligence
ML	Machine Learning
RMSE	Root Mean Squared Error
PVD	Physical Vapor Deposition
SEM	Scanning Electron Microscope
EDX	Energy-Dispersive X-ray Spectroscopy
ICP-MS	Inductively Coupled Plasma Mass Spectrometer
XPS	X-Ray Photoelectron Spectrometer
GIXRD	Grazing Incidence X-Ray Diffraction
XRD	X-Ray Diffractometer
AFM	Atomic Force Microscope

Chapter 1:
INTRODUCTION

1.1 High entropy alloys

1.1.1 Concepts and background

Since ancient times, humans have been changing the properties of the material by adding alloying elements. Despite pure metals utilization in some specific applications, alloying elements are generally added to enhance the physical or chemical properties. Thus, most practical alloys are multicomponent elements [1]. In 2004, the first HEA paper published by Huang and coworkers [2] introduced a new alloy concept as multi-principal-element alloys (MPEAs) in order to combine both oxidation and wear resistance properties. The XRD results exhibited one ordered BCC phase and two FCC phases, not expected since multi principal alloys tend to form complex compounds with many alloying elements. Consequently, MPEAs were proposed as promising candidates for high temperature oxidation and abrasion.

The two independent publications by Jien-Wei Yeh [3] alongside Brian Cantor [4] in 2004, introduced a new alloy concept as "high-entropy alloys (HEAs)" or "multi-principal element alloys (MPEAs)," which were published by other researchers in the same year as well [2, 5-7]. Yeh and coworkers hypothesized that mixing multiple elements (more than five) in relatively high concentrations, mostly equiatomic, results in high configurational entropy of mixing, preventing harmful intermetallics from forming. An alloy created by adding pure elements can form solid solution or compounds which their free energies are calculated by following equations [8]:

$$\Delta G_{mix} = \Delta H_{mix} - T\Delta S_{mix} \quad (1)$$

$$\Delta G_f = \Delta H_f - \Delta S_f \quad (2)$$

Where ΔG_{mix}, ΔH_{mix}, and ΔS_{mix} are the Gibbs free energy, enthalpy, and entropy of mixing, respectively; ΔG_f, ΔH_f, and ΔS_f are the corresponding values for the formation of an intermetallic compound. Following Boltzmann's hypothesis [9], the mixing entropy and system complexity may be calculated by:

$$\Delta S_{\text{conf}} = -k \ln \omega = R \ln n \quad (3)$$

Where k is Boltzmann's constant, ω is the number of the ways of mixing, R is the gas constant, and n is the number of elements. For example, ΔS_{conf} for alloys with 3, 5, 6, and 9 elements are 1.10R, 1.61R, 1.79R, and 2.20R, respectively [3]. Assuming the solid solution is in ideal condition and the intermetallic compound in perfect order for simplification, the relative stabilities of solid solution and intermetallic compounds depend on whether $-T\Delta S_{mix}$ is more negative than ΔH_f or not. Consequently, an alloy comprising a higher number of alloying elements increases configurational entropy of mixing, sufficient to form solid solution rather than intermetallic compounds except for those with very large heats of formation. Contrary to the conventional opinion that a higher number of principle elements increase the chance of forming compounds, it was shown that the entropic contribution to the total free energy would overcome enthalpic contribution, and thus solid solutions stabilize.

According to Yeh [10], the extraordinary properties of high entropy alloys arise from four core effects which are: (i) high entropy effect, (ii) severe lattice distortion, (iii) sluggish diffusion, and (iv) cocktail effect. The high entropy effect is where alloys containing multiple elements tend to form solid solution rather than intermetallic due to high mixing entropy, as mentioned before. Different atomic sizes and bonding cause the lattice distortion effect shown in Figure *1.1* in a multi-element crystal of HEA, which results in solution hardening the crystal and enhancing properties such as strength and hardness [11]. The sluggish diffusion effect results in higher diffusion, leading to higher recrystallization temperatures, creep resistances, and slower grain growth [12]. It is caused due to the limitation of diffusion in the HEAs, which hinders the atomic movements. Finally, the cocktail effect is where the HEAs act as an atomic-scale composite and exhibit composite effects coming from the basic features and interactions among all the consisting elements. Consequently, it implies that alloy properties can be adjusted by changing the alloying elements and compositions. For instance, Figure *1.2* [3] indicated the hardness change of the alloy by changing the Al content in the alloy. HEAs became a strong candidate at various technical and biomedical applications due to their superior mechanical properties such as strength and hardness [13-15], tribological properties [16], excellent corrosion resistance [17, 18] and high hardness and wear resistance [19, 20].

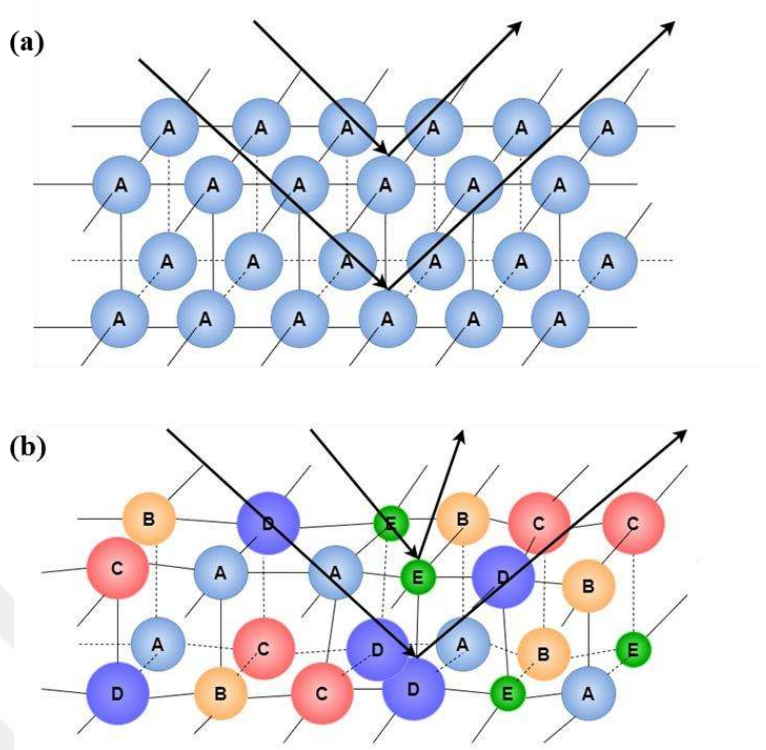

Figure 1.1 Schematic illustration of the lattice distortion effects on Bragg diffraction: (a) perfect lattice with the same atoms; (b) distorted lattice with solid solutions of different-sized atoms, which are expected to be randomly distributed in the crystal lattice.

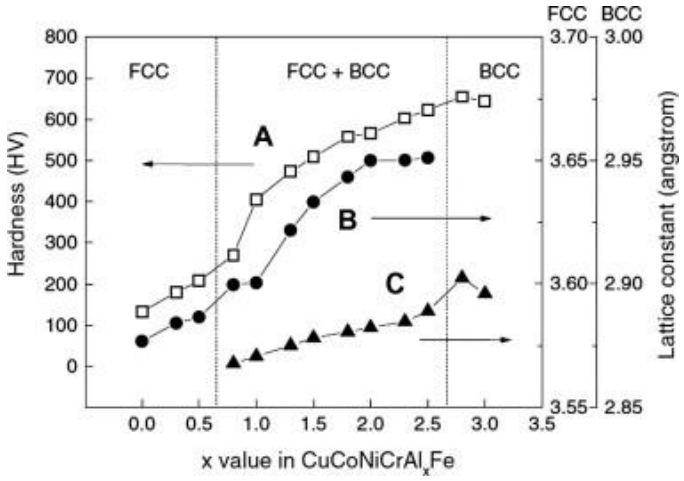

Figure 1.2: Hardness and lattice constants of a CuCoNiCrAl$_x$Fe alloy system with different x values: (A) hardness of CuCoNiCrAl$_x$Fe alloys, (B) lattice constants of an FCC phase, (C) lattice constants of a BCC phase

1.1.2 Applications and motivation

Metals such as Ti-based alloys, Co-based alloys, and stainless steel are commonly preferred for biomaterials owing to their enhanced properties such as excellent mechanical properties and biocompatibility [21]. They are mainly used in implants such as artificial hip joints, artificial knee joints, bone plates, and dental implants. However, non-toxic alloying elements are selected for such applications; metal allergy and toxic ion release, tissue loss, or modulus mismatch are still common problems. For instance, Ni ion release from NiTi shape memory alloys into tissue or blood [22], or V and Al ion release from the famous Ti-6Al-4V alloy, which damages the nervous system and raises high-risk health issues [23]. Co, Cr, and Ni were pointed out as highly allergic alloying elements, while Nb, Ta, and Zr were judged to be non-toxic and safest alloying elements [24].

Consequently, researchers still look for alternative metallic implant candidates with excellent biocompatibility and mechanical properties. In addition to HEA applications as novel metallic functional materials, high entropy alloys also attracted attention in biomedical applications [25]. Novel biomedical high entropy alloys started to develop to tackle the problems of commons metallic biomaterials. One of the causes of implants loosening and failure is the stress shielding effect caused by stress reduction in bone since the implant bears most of the applied load. As a result, the implant is preferred with a low modulus of elasticity in order to decrease the stress shielding effect. One of the characteristics of HEAs is adjusting the modulus by adjusting the composition and elements of comprising alloying elements [26], providing an opportunity for designing desired biomaterials with low modulus. HEAs are among the materials with highest specific strength and with a wide range of Young's modulus.

This unique combination of features encouraged researchers to investigate these alloys in biomedical applications. HEAs containing Ti, Ta, Nb, Mo, and Zr are extensively investigated by researchers [27-30] in biomedical applications. Gurel et al. performed static immersion experiments in SBF and AS solutions on TiTaHfNb, TiTaHfNbZr, and TiTaHfMoZr alloys. The experiments revealed enhanced long-term corrosion resistance due to forming a protective passive layer on the surfaces with low ion release, indicating the potential of these alloys in biomedical applications [16]. Another study on the in vivo biocompatibility tests on TiZrNbTaMo showed no signs of

toxic response and excellent corrosion resistance [31]. Eventually, Hf was also proposed as another potential alloying element because of good biocompatibility and osteogenesis confirmed by implantation [32]. Yuan et al. developed the TiZrHfNbTa HEAs, consisting of five elements proven to be non-toxic and favorable to form a solid solution with a unique combination of low modulus and good mechanical biocompatibility [33]. In another study, the corrosion behavior of the two alloys of TiTaHfNbZr and $Ti_{1.5}ZrTa_{0.5}Hf_{0.5}Nb_{0.5}$ were experimentally tested and compared with 316 L stainless steel, CoCrMo, and Ti6Al4V alloys, which manifested considerably higher corrosion resistance [14]. $Ti_{1.5}ZrTa_{0.5}Hf_{0.5}Nb_{0.5}$ had thicker corrosion-resistant barrier oxide film attributed to a higher amount of electronegative Ti and Zr elements. Nagase and coworkers developed TiZrHfCrMo and TiZrHfCoCrMo as potential candidates for orthopedic implants with improved mechanical hardness and biocompatibility [34].

Despite all research done to design a high entropy alloy with excellent biocompatibility, there is still room for improvement. The properties of HEAs affecting the final biocompatibility of the designed alloy can be manipulated by choosing and changing the alloying elements and their compositions. Each including an element in the alloy has the effect by itself and on the other elements as well. Due to the complexity of considering all the crucial parameters and the number of possible combinations, one efficient way to tackle this problem is using computational algorithms. This compositional space allows challenging optimization processes that are not easy to solve by conventional experimental methods or trial and error. Several computational methods have been used for guiding the alloy design of high entropy alloys, such as thermodynamic modeling, density functional theory (DFT), and molecular dynamics (MD) [35-38]. CALPHAD is mainly used to predict the phase formations [39], while DFT and MD mainly focus on phase stability and solidification of HEAs.

Alloy design with preferred properties can be reached by modifying chemical compositions that can control the microstructures and phase formation [40]. Consequently, the number of alloying elements and the variety of microstructures and resulting features give rise to complex computations. As an alternative solution, machine learning (ML) tools have begun to utilize materials science researchers [41, 42]. Tepla et al. developed a logistic regression method from ML tools with an overall accuracy of 96.7% based on the ratio of correctly classified titanium alloys to design biocompatible titanium alloys [43]. In one study, the corrosion rate of steel alloys was predicted by

machine learning tools by using the chemical composition and environmental factors as input data [44]. For HEAs, a property-oriented method based on machine learning was proposed by Cheng et al. to find high hardness values alloys [45]. Many investigations have been done on phase formation of high entropy alloys by implementing ML methods [46-48]. For instance, Islam et al. developed an ML model that can classify the phase selection in HEAs by finding the pattern underlying the available experimental dataset. Their model also suggested that the valence electron concentration has the most essential effect on the resulting phases [49]. These examples demonstrate the promising applications of machine learning tools in property selection and alloy design while being timely and costly efficient.

In the present study, we proposed a property-oriented alloy design by machine learning algorithms. The purpose of this work is to find a new alloy containing non-toxic metals with enhanced biocompatibility and mechanical properties. To do that, firstly, a comprehensive dataset including physical, chemical, and biocompatibility properties of metals was extracted from literature. Then a well-established unsupervised machine learning method named clustering was used to cluster the metal candidates. The quality and accuracy of the clustering algorithm were then evaluated and reported, which indicated the high performance of the model. Among the predicted clusters, one of the clusters containing the elements with the highest biocompatibility was selected to be made. This alloy will be examined experimentally to validate the model results and to be used as a potential implant later.

1.2 Machine learning

1.2.1 Definition and concepts

In case of encountering a new situation, humans tend to make decisions based on similar past experiences. The decisions will improve as similar experiences increase. Artificial intelligence and machine learning recently utilized the same concept to learn and predict based on existing (training) data rather than solving via experiments or computations [41]. Machine learning uses statistics in building mathematical models to optimize performance using example data and past experiences. To make such a system intelligent, it should have the ability to learn and adapt to a changing environment. Firstly, the training step stores and processes massive amounts of data and then solves the

optimization problem by efficient algorithms. Then, after the model is constructed, the representation and solution need to be efficient and space and time complexity.

Some examples of such machine learning models are facial recognition or self-driving cars developed by gathering data from past scenarios. One of the essential aspects of machine learning is the way it deals with the input data. A numerical way is required to quantitatively predict the results from the inputs, which mainly functions iteratively based on the correlations between the inputs and targets. Machine learning applications to large databases are called data mining, which means when a large amount of data is processed to construct a model with high predictive accuracy [50], for instance, learning models for banks by using their past data in the stock market. Another example in manufacturing is models to optimize the production process and troubleshoot.

In general, ML algorithms can be categorized into classification or regression models. In regression problems, the model predicts continuous values for the output, which is a number such as predicting the price of a car. In contrast, classification problems predict discrete output values, such as categorizing the input values, for example, predicting whether an email is a spam or not [50]. In another approach, ML training methods can be divided into three groups of supervised, semi-supervised, or unsupervised learning, based on the type of available data [51]. In supervised learning, the training data consist of input and output values, and the goal is to derive functions on input values which results in the prediction of the output values with acceptable accuracy. Semi-supervised learning is when there is a large amount of input data with limited corresponding output data. In the case of unsupervised learning, the available dataset only consists of input data, and the goal of the algorithm is generally to find regularity in input data, such as clustering the data or identifying trends and patterns among them. It tries to find a structure in input such that particular patterns occur more often than others, referred to as density estimation in statistics. One method of density estimation is clustering which the aim is to cluster similar inputs in the same groups.

1.2.2 Clustering algorithms

Clustering algorithms arise as one of the rich conceptual frameworks of unsupervised learning, which discover structures in data. The clustering task can be challenging both conceptually and computationally. As the name implies, it is anticipated

to explore similarities or differences between individual data points in a data set [52]. There are various strategies for cluster formation and determining the meaning of similarity in the data, addressing different facets and properties of clusters. Clustering techniques can be categorized into three main groups of partition clustering, model-based clustering, and hierarchical clustering.

In partition-based clustering, a specific objective function discovers the structure existing in the data with a predefined number of clusters. In this case, the expected type of the structure is uncertain and hence the most suitable objective function [52]. In model-based clustering, a certain probabilistic model of the data is assumed, and then the parameters are estimated. The model is a mixture density model in which the data are assumed from sources that each source will be assumed as a potential cluster. Hierarchical clustering is a successive development of clusters that is categorized into two different processes of finding clusters. In one way, all the data points are treated as one cluster then being divided into more. In another way called agglomerative clustering, each data point is treated as a cluster and then merged based on the distance between data and patterns. As with many other multivariate techniques, agglomerative hierarchical clustering is carried out on a set of variables on the rows of an array or matrix [53]. This method uses a bottom-up approach meaning that each observation starts in its cluster and then successively merges. The linkage criteria determine the metric used for the merge strategy.

1.2.3 Hierarchical/agglomerative clustering

Since the 1970s, it has been held that around 75% of published works on clustering algorithms employed hierarchical clustering algorithms [54]. A common interpretation of hierarchical clustering is to detect partitions or levels of hierarchy. Hierarchical clustering is one of the essential and well-established methods of unsupervised machine learning. Initially, each input is considered a singleton node, then merges and agglomerates step by step the current pair of mutually closest nodes into a new cluster until there is no node left. Various clustering schemes calculate the inter-cluster dissimilarity after each step which the most common methods are single, average, complete, and Ward linkage, as shown in Table 1.1 [55]. These techniques are implemented in standard numerical and statistical software such as MATLAB and Python [56]. The algorithm starts with a forest

of clusters that will be later used to form the hierarchy. When two clusters merge into a single cluster, the first two are removed from the forest, and the new one is added. This process will continue until only one cluster remains, which becomes the root. The distance matrix is computed including the distance between clusters of the original forest. The algorithm is updated at each iteration to reflect the distance of newly formed clusters with the remaining clusters in the forest. A similarity between a pair of vectors or points is given by: In the case of calculating the distance in a vector space, a traditional method to measure the distance is a Minkovski distance which is a family of metrics calculated as follows [53]:

$$L_p(x_a, x_b) = \left(\sum_{i=1}^{n} |x_{i,a} - x_{i,b}|^p\right)^{\frac{1}{p}};\ \forall p \geq, p \in Z^+ \tag{4}$$

Table 1.1: Agglomerative clustering schemes

Name	Distance update formula for d (I ∪ J, K)	Cluster dissimilarity between clusters A and B
single	min (*d (I, K), d (J, K)*)	min *d* [*a, b*]
complete	max (*d (I, K), d (J, K)*)	max *d* [*a, b*]
average	$\frac{n_I d(I,K) + n_J d(J,K)}{n_I + n_J}$	$\frac{1}{\lvert A\rvert\lvert B\rvert}\sum_{a \in A}\sum_{b \in B} d[a,b]$
Ward	$\sqrt{\frac{n_I + n_k\, d(I,K) + (n_j + n_k) d(J,K) - n_k d(I,J)}{n_I + n_j + n_K}}$	$\sqrt{\frac{2\lvert A\rvert\lvert B\rvert}{\lvert A\rvert + \lvert B\rvert}}.\ \lVert c_A - c_B\rVert_2$

The Euclidean distance is a particular case of Minkovski when $P = 2$, which maps the data equiweighted for clustering. The hierarchical algorithm can be visualized by dendrogram graphs, as shown in Figure *1.3*. It does not determine the unique clusters, and the user should choose which of the subtrees are clusters and which ones are only a part of a bigger cluster [57]. A dendrogram collects and gives the classificatory relationships between the data points. It can represent how many functional groups can be found in the data based on the application.

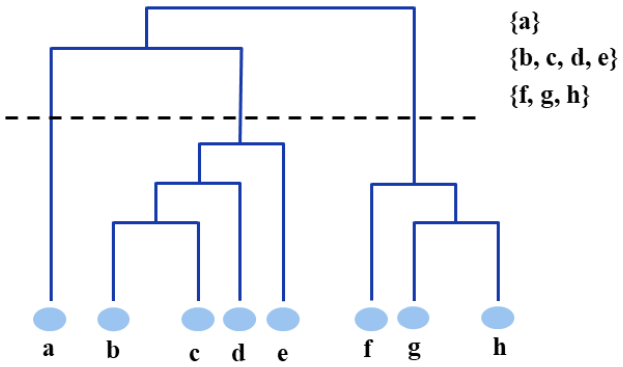

Figure 1.3: A dendrogram for visualization of structure in data

The linkage algorithms shown in Table 1.1 are used to compute the distance between the newly formed and remaining clusters. The single linkage clustering method proposed by Gower and Ross [58] is obtained from a minimum spanning tree (MST) of the weighted graph by the complete graph with the dissimilarities as edge weights. It gives the interconnecting dissimilarity between two clusters as the least interconnecting dissimilarity between a member of one cluster and the other. This is also known as the nearest point algorithm. The complete method is the same as the single method but computes the maximum difference known by the farthest point algorithm or Voor Hees algorithm. The average method equation is given in the table, which is also called UPGMA. Finally, the Ward method uses the Ward variance minimization algorithm, also called an incremental algorithm.

The k-means algorithm assigns data points to a predetermined number of clusters by using distance metrics. It clusters data by separating samples into groups of equal variances, minimizing a criterion known as inertia or within-cluster sum-of-squares [59]. There are several methods available to choose the optimal number of clusters, such as the elbow method and the distance metrics methods. The variance within a cluster and between clusters are given in Eq.5 and Eq.6, respectively. The total variance of the data set is calculated by the addition of variance within the cluster and between the clusters [60].

$$\text{SSW } (C, k) = \sum_{i=1}^{N} \left\| x_i - c_p(i) \right\|^2 \quad (5)$$

$$\text{SSB } (C, k) = \sum_{j=1}^{k} n_j \left\| c_j - x \right\|^2 \quad (6)$$

$$\sigma\ (\text{X}) = \sum_{i=1}^{N} \left\| x_i - c_p(i) \right\|^2 + \sum_{j=1}^{k} n_j \left\| c_j - x \right\|^2 \quad (7)$$

1.3 Coatings concepts and applications

High entropy alloys (HEAs) have been proposed as one of the potential candidates to be used as a metallic biomaterial implant [61, 62]. The biomaterials must have some characteristics such as high corrosion resistance, suitable mechanical properties, and not creating toxic reactions in the human body [63]. HEAs usually consist of four or more elements, which results in high configurational entropy leading to a single stable phase in most cases. That generates excellent corrosion properties, high hardness, and strength, leading numerous studies to investigate HEAs applications in the biomedical field [62]. HEAs consist of non-toxic transition metals such as Ti, Ta, Hf, Mo, Nb, and Zr have been investigated by many authors. These investigations mainly involved the assessment of the metal and fluid changes by immersing the alloys in different corrosive environments such as simulated body fluid (SBF) and artificial saliva (AS) [14, 16]. Metallic implant surfaces can be vulnerable to infection because of biofilm formation at the surface and reduced immune ability at the implant/tissue interfaces [64]. There are still challenges to eliminating infection after inserting the implant, thus removing the implant usually seems the primary way to tackle this issue, and new approaches are required to prevent the bacterial infection.

One of the common methods to introduce antibacterial properties to substrates is coating them with materials that possess antibacterial characteristics. Antibacterial coating prevents the adhesion of bacteria to the surface of the implant or releases antimicrobial agents. Silver has a long history of being used as an antibiotic for human health care. The antimicrobial activity mechanism of silver or silver compounds at low concentrations (<1 ppm) mainly arises from the release of Ag^+ ions to then interact with the bacterial cells [65]. Silver has a broad spectrum of antibacterial characteristics to different kinds of bacteria at very low ppm concentrations [66, 67]. Silver metal ionizes in water or tissue fluids and releases Ag+, which shows a strong affinity. The silver ion

is biologically active and toxic to microorganisms by poisoning the respiratory enzymes and components in the microbial electron transport system [68]. Silver shows low toxicity in the human body since it can be absorbed and eliminated by the liver and kidneys. It confirms the excellent properties of silver to be used in biological and medical applications.

PVD coating process is known as an effective method for coating metals and ceramics and is widely used in technical and medical applications [69]. The coating by PVD method is produced by particles condensation, which are atoms or atom clusters under reduced pressure. These particles are released from the target or source by physical approaches, which are sputtering, evaporation, or resistance heating [70]. In the sputtering method, accelerated Argon ions that are generated in an electromagnetic field strike the target; meanwhile, in the evaporation method, the particles are released inductively by an arc, laser, or electron beam. The ionized released particles react with the atmosphere inside the vacuum chamber and accelerate by the negative bias voltage to the surface of a substrate and form a thin homogenous coating. The film growth generally consists of stages of initial nucleation of the target on the substrate surface, then the growth of the nuclei and formation of islands (often crystallites), formation of a connected network by merging the islands, and at last filling the channels [71].

By adjusting the sputtering factors and substrate conditions, a various range of coating structures can be obtained. Parameters during sputtering which can generally impact the coating morphology are: (i) kinetic energy of the sputtered particles, (ii) plasma conditions, (iii) surface topography, and (v) substrate temperature [72]. Another study revealed the effects of pressure and power during sputtering on the surface diffusion of the Ag atom into the growing film. They showed that as the power decreases and pressure increases, the surface diffusion increases, which can enhance the growth of islands at the first stage of growth and delay the formation of a homogenous film [73]. By decreasing the Argon pressure during the coating, the condensed silver atoms on the film might possess sufficient kinetic energy to move on the surface and therefore favoring the grain growth [74].

1.4 Objectives

In this study, computational and experimental methods were implemented to enhance the biocompatibility of high entropy alloys. In the second chapter, the ML method is implemented in order to reveal the best combination of elements of a high entropy alloy with biocompatibility properties. The hierarchical clustering and k-means method were used and compared for grouping of the biocompatible metallic elements. Using the already published articles and handbooks, the most effective chemical, physical, and mechanical features of metals are gathered and used as the input data. Consequently, a HEA comprising of six elements was predicted and evaluated by unsupervised machine learning methods. In the third chapter, silver coatings are deposited on three different high entropy alloy substrates at three different thicknesses by adjusting the PVD process parameters. The coatings are aimed to provide antibacterial properties to the alloy by releasing silver ions into the aqueous environment while maintaining the biocompatibility and mechanical characteristics of the HEA substrates. Another aim is also to prevent the ion release of the substrate elements and minimize the toxic reactions. As a result, the coatings homogeneity and ion release of both substrates and coatings were measured and reported.

Chapter 2:
BIOCOMPATIBLE HIGH ENTROPY ALLOY DESIGN BY CLUSTERING ALGORITHMS

This chapter has developed an artificial intelligence framework to categorize the most similar elements in the same group based on their physical and chemical properties, including three main steps. Firstly, the data set comprising of metal candidates and their features are gathered. Then, the features are scaled in order to be able to be used by the ML method in the same weight. Finally, the cluster features such as compactness and similarity are assessed by measuring relevant metrics.

2.1 Data collection and feature generation

The experimental data of 32 pure metals as potential alloying element candidates, which have been proven to show biocompatibility, have been extracted from the literature. The candidates are Rb, Cs, Be, Sr, Ba, Y, Ti, Zr, Hf, V, Nb, Ta, Cr, Mo, W, Mn, Fe, Ru, Co, Rh, Ir, Ni, Pd, Cu, Ag, Zn, Cd, Al, In, Sn, Sb, and Bi. The ten elemental properties shown in Table *2.1* were selected based on their effect on the biocompatibility properties of the final alloy. The mechanical properties of the alloy have a crucial impact on the choice of elements since it might be one of the main reasons for implant failure. For instance, the alloy used as an implant should have modulus close to the bone, or else it might cause a stress-shield effect.

Consequently, Young's modulus and Poisson's ratio of the candidates have been gathered as inputs for this work [75, 76]. Metallic biomaterials may corrode and release metal ions inside the body, which might cause toxic reactions on the tissues and organs. In order to assess the biocompatibility of the metals, the cytotoxicity of the metal salts has been evaluated by the colony formation method using two kinds of cultured cells, L929 and MC3T3. The metal's salts relative cytotoxicity have been gathered from literature indicated as IC_{50} that is also known as inhibitive concentration [77].

Table 2.1: The features gathered for this study

Elemental Properties
Surface Energy
Melting Point
Density
Young's Modulus
Poisson's Ratio
Atomic Radius
Pauling Electronegativity
Number of valence electrons
IC_{50}-L929
IC_{50}-MC3T3

In addition to the mechanical and cytotoxicity properties, physical and chemical features of the metals were also added as input features. Since the final alloy's purpose is to form a high entropy alloy, the properties that increase the solubility and phase stability are considered as well. These features are given by the Hume-Rothery rule, which are atomic radius, valance electrons, and electronegativity [78], which are collected from literature and added to the input of this work as well [79, 80]. It has also been reported that reducing the number of valance electrons through controlled alloying was effective in decreasing the modulus [33]. The surface energy (It is chosen for the close-packed plane of each lattice structure. (111 for fcc, 110 for bcc, and 0001 for hcp)) [81], density, and melting points, were also gathered as input features [75].

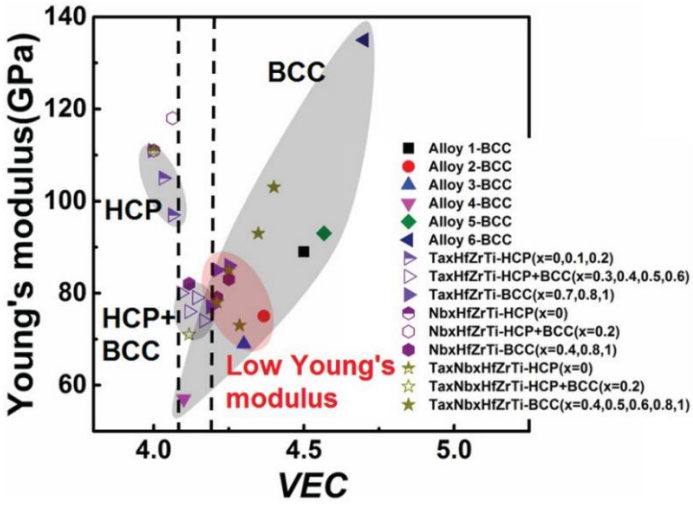

Figure 2.1: Dependence of Young's modulus and crystalline phase structure on VEC in all the HEAs investigated [33].

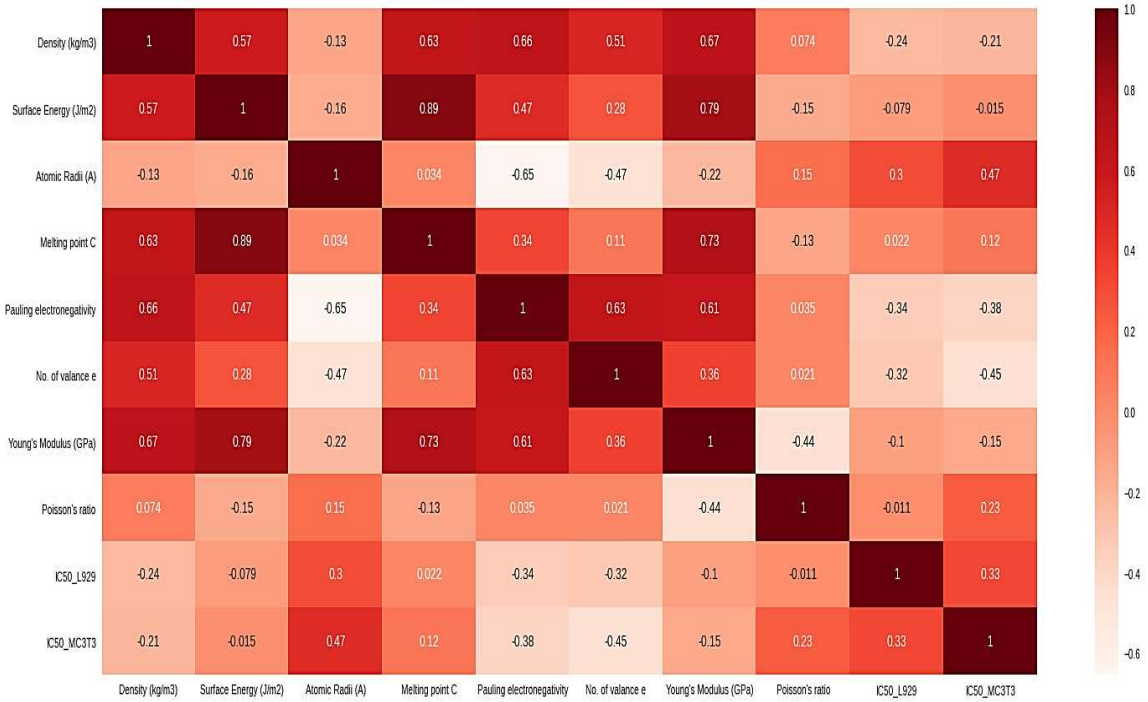

Figure 2.2: Feature correlations shown by different colors. The darker color indicates a higher correlation between the two features.

The features correlation has been calculated by python libraries which are shown in Figure 2.2. As can be seen from the values, no specific correlation is seen among the features, and as a result, all features were used as an input without using any dimension reduction methods.

2.2 Preprocessing of the data

In order to consider all of the features equally and increase the performance of the machine learning algorithms, a preprocessing step on the input data is necessary. That means the values for all features must be transformed to the same scale, which is known as feature scaling. The feature scaling is significant for distance-based machine learning algorithms such as clustering since it can have a significant impact on the performance of the algorithm.

The relevant statistics compute scaling and clustering on each feature of the dataset independently and then store the mean and standard deviation to be used on later data by using the transform method. Four of the most common feature scaling methods that are used in this study are calculated by Sci-Kit to learn package of Python programming, which are summarized as follows [82]:

1) The StandardScaler, or known as standardization, scales the values in a way that the features will have a mean of 0 and a standard deviation of 1.

2) The MinMaxScaler implements a type of feature scaling to a given range that can be set by the feature range parameter (default is between 0 and 1). This scaler is mainly used for a type of data with low standard deviation or no Gaussian distribution, so it is sensitive to outliers.

3) Normalization processes the scaling of the samples to have unit norm. It is mainly used when the algorithm tries to predict based on the weighted relationships between data points. It has three different methods to calculate the norm, which is by using the sum of all the values, using the square root of the sum of all the squared values, or using the absolute maximum.

4) Power Transformers are a family of parametric scaling functions that transform any distribution of data to a nearly Gaussian distribution in order to reduce skewness and stabilize the variance. One of the common functions of power transformation scaling is Yeo-Johnson which is calculated as follows:

$$\psi^{(k)}=\begin{cases} [(x+1)^{\lambda}\{log(x+1)\}^{k}-k\psi^{(k-1)}]/\lambda & (\lambda\neq 0,\ x\geq 0),\\ \{log(x+1)\}^{k+1}/(k+1) & (\lambda=2,\ x\geq 0),\\ -[(-x+1)^{2-\lambda}\{-log(-x+1)\}^{k}-k\psi^{(k-1)}]/(2-\lambda) & (\lambda\neq 0,\ x\geq 0),\\ \{-log(-x+1)\}^{k+1}/(k+1) & (\lambda=2,\ x\geq 0), \end{cases} \tag{8}$$

The transformation is parameterized by λ as the power parameter, which is determined through maximum likelihood estimation. All the scaling as mentioned above methods have been performed on the data set of this study, and the power transformer was chosen to be used as the most suitable function. This scaler is a non-linear transformer that is suitable for a dataset whose difference is in order of magnitude, which is the case of this study.

2.3 Hierarchical clustering results

Modern advanced materials require multiple features in order to achieve better performances than the previous generation of materials. To be able to investigate all the necessary features affecting the final goal of the alloy, clustering from ML algorithms were performed on the gathered elemental properties. In order to investigate the trends and underlying patterns in the dataset, several visualizations and clustering techniques were applied to the data, which were hierarchical and K-means clustering algorithms. A cluster consists of data points similar to each other, while the data points of one cluster are different from the other one. This similarity can be calculated by different methods which the most common one is Euclidean distance [83]. In HCA, clustering begins as one cluster for each data point, then they merge iteratively and finally become one large cluster. In this work, following the data gathering and pre-processing of features, the clustering was performed by Ward approach as a tree-like structure known as dendrogram that indicated how the clusters are related to each other and the whole process is schematically shown in Figure 2.3.

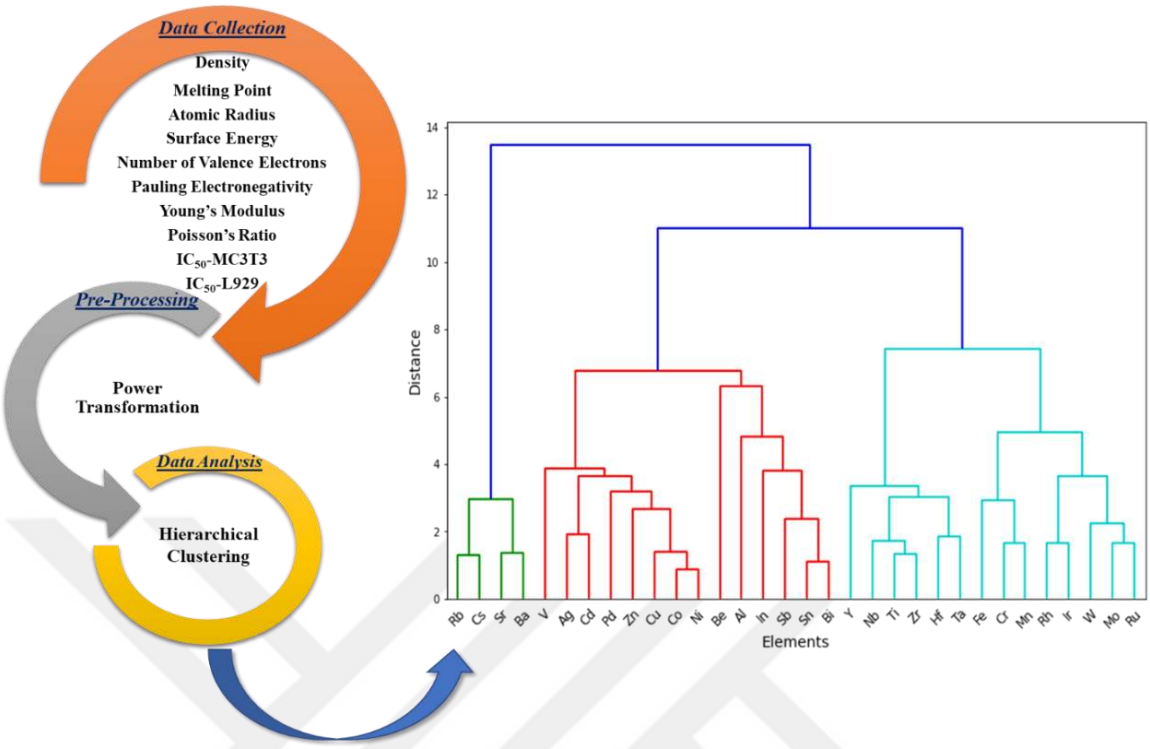

Figure 2.3: Schematic of the ML procedure proposed in this study for alloy design

The elements are clustered based on the ten input features, including numerical values of physical, chemical, and mechanical properties of pure metals. The dendrogram can be cut at any distance based on the purpose of the study, which will define the number of clusters that are chosen. As it can be seen from Figure 2.4, 5 main clusters were chosen as the alloy candidates of this study. This figure also represents the clear difference between clustering results prior to and after the data pre-processing. It can be seen that by scaling the data, the clusters cohesion and separation enhanced dramatically. To peak the cluster that includes the best combination of elements, a literature review was done in order to select a cluster that all of the members are biocompatible. Ti, Ta, Hf, Nb, and Zr are already proven to have biocompatible properties, and they have been suggested as the biomedical high entropy alloys in the previous studies [14, 16]. They exhibited excellent corrosion resistance and mechanical properties and were proposed as a potential candidate for biomedical applications. Consequently, the cluster including those elements was selected as the target alloy, which is also including Y as the sixth element.

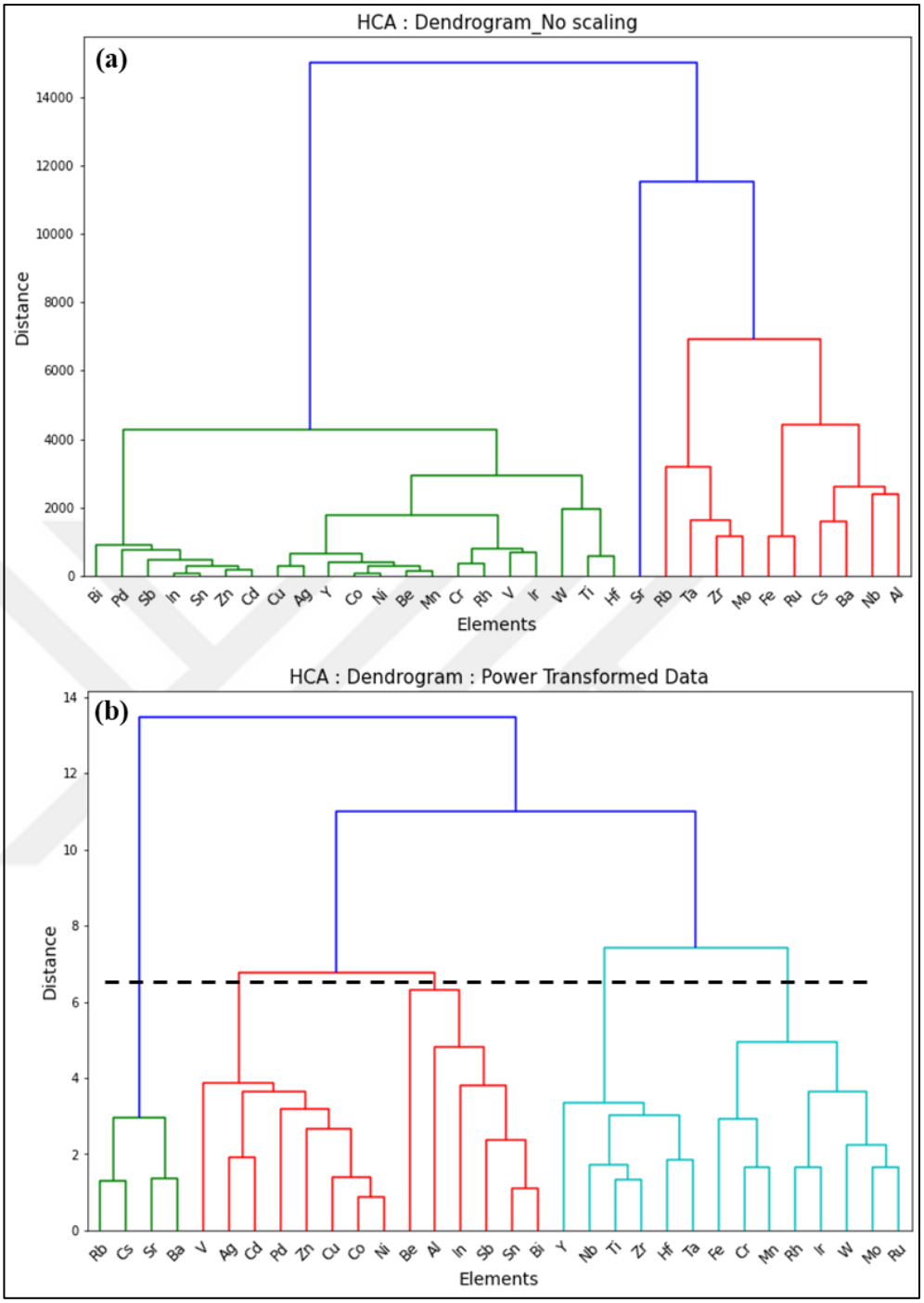

Figure 2.4: Dendrogram plots from HCA analysis on (a) non scaled input features (b) Power transformed input features

In addition to HCA, a K-means clustering algorithm was also performed on the data points to group the most similar elements in order to define the new biomedical high entropy alloy. The K-means algorithm defines the initial centroids, which will become the new mean until converging to clusters. It calculates the summation of squared distance between all centroids and data points, then assigns each data point to the nearest centroid

(cluster). Then it computes the new cluster centroid through the average of all data points belonging to each cluster. Then the nearest data sets generated will be grouped by similar data points, and these steps are repeated until the iterations are converged [60]. Since the K-means algorithm requires a predefined number of clusters, it was set at 5 in order to result in an alloy with at least six elements. The results yielded from this algorithm on the data points of this study that were firstly scaled by power transformer function are tabulated in Table *2.2* below.

Table 2.2: K-means clustering results

Cluster number	Elements
Cluster 1	Ti, Ta, Nb, Hf, Zr,Y, Fe,Al
Cluster 2	Rb, Cs, Sr, Ba
Cluster 3	Be, V, Cr, Mn, Co, Ni
Cluster 4	Mo, W, Ru, Rh, Ir
Cluster 5	Pd, Cu, Ag, Zn, Cd, In, Sn, Sb, Bi

As it can be seen, cluster 1 illustrates the same configuration of elements as the HCA except including Fe and Al in the cluster as well. Since the toxic effects of Fe and Al on the human body have been proved by many studies before, Yttrium has been chosen as the best candidate for the alloy design as the HCA also proved it. Previous work by authors has investigated the effects of small additions of rare earth elements such as Yttrium in the range between 0.1 to 1 wt.% to a Titanium alloy, which resulted in reducing Young's modulus and significantly improving the fatigue resistance [84]. In other works, Y addition reduced the average grain size and thus increased the strength; it also proved to be beneficial in terms of scavenging oxygen and enhancing fracture toughness [85, 86]. Consequently, one wt.% of Yttrium was decided to be added to an equimolar amount of Ti, Ta, Hf, Nb, and Zr produced by vacuum are melting. The alloy will be tested in terms of mechanical and biocompatibility properties as the ultimate goal of this work.

2.4 Clustering Evaluation

Many authors tried to investigate how to evaluate the features of a desirable clustering algorithm. The quality of the results obtained by clustering techniques has been one of the challenges of unsupervised learning algorithms. As a result, many studies

proposed various techniques to evaluate the quality of clustering depending on the clustering method and the cluster data type. The evaluation techniques can be categorized into two main groups of internal and external similarities [83]. The internal similarity reflects the compactness of a cluster that higher shows better compactness. The external similarity indicates the uniqueness of a cluster that should be lower. The relevant variables that help to identify cluster elements can be referred to as descriptive and discriminating variables. The first one indicates the cluster elements like each other, and the latter one identifies the dissimilar clusters.

One of the common evaluation coefficients of hierarchical clustering algorithm is the cophenetic correlation distance between two examples which calculates the proximity at an agglomerative hierarchical clustering algorithm that puts the data points at the same cluster [87]. This metric is used for evaluating the results of the hierarchical clustering algorithm. In a dendrogram, it corresponds to the height at which the branches corresponding to the two examples are merged. [88] This value is between -1 and 1, and a higher value indicates that the clustering algorithm was able to identify the underlying structure of the input data more successfully. The cophenetic correlation coefficient is then calculated by:

$$\mathrm{CPCC} = \frac{\sum_{i<j}(\mathrm{d_{ij}} - \mathrm{d})(\mathrm{d}^{*}_{ij} - \mathrm{d}^{*})}{\sqrt{\sum_{i<j}\left(\mathrm{d}_{ij} - \mathrm{d}\right)^{2} \sum_{i<\mathrm{j}}\left(\mathrm{d}^{*}_{ij} - \mathrm{d}^{*}\right)^{2}}} \tag{9}$$

Where d_{ij} is the distance between the example pair (i, j) and d^*_{ij} is their cophenetic distance. The correlation coefficient also includes the average d of the distances in the proximity matrix and the average d* of the cophenetic distances in the cophenetic matrix. The cophenetic metric measured for this study was calculated as 0.674, which is an indication of the high ability of the clustering model for identifying the underlying structure of the data set.

The silhouette coefficient measures the cohesion and separation of clusters. It indicates how well a data point fits into its assigned cluster based on how close it is to the other data points of its cluster and how far it is from the points of the other clusters [88]. The computing silhouette coefficient of a particular point consists of the following three steps:

i. The average distance to all examples in the same cluster calculates as follows:

$$a(i) = \frac{1}{|c_a|} \sum d(i,j) \tag{10}$$

ii. The minimum average distance between a data point and other data points of the other clusters is computed as follows:

$$b(i) = \min \frac{1}{c_b} \sum d(i,j) \tag{11}$$

iii. For each data point, the silhouette is defined by the following expression:

$$s(i) = \frac{b(i) - a(i)}{\max\{a(i), b(i)\}} \tag{12}$$

The global silhouette coefficient is determined by taking the average of the particular silhouette coefficient of each data point as indicated below:

$$S = \frac{1}{n} \sum_{i=0}^{n} s(i) \tag{13}$$

This coefficient is also ranging between -1 and 1, in which larger values indicate that data points are closer to their own clusters than they are to other clusters. When the silhouette value is zero, it means that the data are uniformly distributed toward the Euclidean distance. Negative values show that the clusters are mixed with each other, and positive values are an indication of a high separation between clusters. In the current work, the silhouette values were 0.24 and 0.23 for the HCA algorithm and K-means algorithms, respectively, which indicated the relatively high separation of the clusters.

The Calinski-Harabasz coefficient (CH), which is also known as the variance ratio criterion, is based on the internal dispersion and the dispersion among the clusters [89]. This coefficient is calculated by dividing the variance of the sums of squares of the distances of each data point to their cluster center by the sum of squares of the distance between the cluster centers. The Calinski-Harabasz coefficient is given by the following expression:

$$CH = \frac{BCSM}{k-1} \cdot \frac{n-k}{WCSM} \tag{14}$$

Where k is the number of clusters, n is the number of records in data, BCSM (between cluster scatter matrix) calculates separation between clusters, and WCSM (within-cluster

scatter matrix) calculates compactness within clusters. This value does not have a specific range, and the higher value indicates the better clustering model. For the current study, this score is calculated as 11.52 and 11.62 for the HCA algorithm and K-means algorithms, respectively.

2.5 Conclusions and future work

Hierarchical clustering algorithm and K-means algorithm were utilized in this study to predict a new high entropy alloy consisting of 6 elements for biomedical applications. The most essential physical, chemical, and mechanical properties of metal candidates were gathered from literature to be used as the input of the models. Both models predicted that TiTaHfNbZrY might be the best candidate among the other combinations. The accuracy of the clustering algorithms was evaluated by the most common unsupervised machine learning evaluation metrics, which showed the high performance of both of the clustering techniques. Finally, the predicted alloy by clustering algorithms will be examined experimentally to validate the ML model's prediction accuracy, which will be reported later. In order to enhance the biocompatibility properties of mentioned HEAs, an experimental method was also implemented in this study. Three different HEAs containing different configuration of same elements from ML model chosen elements were used as substrates for coating experiments that is explained in the following chapter.

Chapter 3:

MICROSTRUCTURAL AND BIOCOMPATIBILITY ASSESSMENT OF SILVER COATINGS DEPOSITED ON HIGH ENTROPY ALLOYS

3.1 Introduction

The high entropy alloys are defined as alloys that contain at least five different elements at ranges between 5 and 35 %, which increase the probability of forming one solid solution due to high mixing entropy [3]. These alloys possess unique properties such as excellent corrosion resistance and good mechanical properties, giving rise to various technical and medical applications. Several biomedical-oriented HEAs are now being developed with a broad spectrum of possible compositions. High entropy alloys containing non-toxic elements have been investigated by many authors and thus proposed as a promising candidate to be used in biomedical applications [61]. Their biocompatibility has been experimentally tested by immersing them in simulated body fluids, indicating their great potential to be used as an implant inside the human body [16].

Despite their biocompatible properties, implants are susceptive to bacterial infections after implantation inside the body due to various reasons such as contamination of the implant's surface or formation of resistant biofilms [69]. The post-operative infections can be overcome or reduced by adjusting the antimicrobial properties of the implant surface before implantation. One of the most common metals for antimicrobial application is silver due to the antibacterial activity of silver ions and being non-toxic to human cells [90]. Authors have also shown that silver possesses anti-inflammatory properties and can improve healing rates [91]. Silver ions are effective for most bacterial infections, except a few ones that make it one of the best candidates to be used in such applications. Silver can inhibit the bacteria attachment onto biomaterials, and it also has a long-lasting effect. In vitro investigations demonstrated no cytotoxicity and genotoxicity from silver coatings [64]. Since silver is relatively stable, it can be applied by many well-established techniques such as ion implantation, PVD, and sputtering. Many studies have used radio frequency magnetron sputtering for silver coatings [92]. The sputtering deposition is a well-known physical vapor deposition method under

appropriate deposition conditions. The sputtering parameters such as deposition time, sputtering power, or gas pressure can affect the coating quality and thus the antibacterial properties of silver [93].

The present study was done to introduce antibacterial characteristics to biomedical high entropy alloys and decrease the ion release of HEAs elements employing the PVD process. Silver was coated on three different high entropy alloys at three different thicknesses by adjusting the PVD device parameters. The coated substrates were then subjected to body fluid immersion tests in order to measure their ion release quantitatively in addition to their microstructural properties. The results indicated that by increasing the deposition duration from 20 minutes to 60 minutes, the coating thickness increased from 360 nm to 1 µm. By increasing the coating thickness, the films became denser, and significant grain growth of silver occurred. Such changes can affect the antibacterial properties since it depends on the coating properties. The ion release of films on the three HEA substrates was measured by ICP-MS for three coating durations which indicated that.

3.2 Materials and methods

The silver target was prepared by vacuum arc melting with 99.99% purity in the form of a disk with a diameter of 50.8 mm and a thickness of 6.3 mm. Three different high entropy alloy substrates with 99.9% purity and compositions shown in Table 3.1 were produced by vacuum arc melting method with thicknesses of 6.1 mm and 50.1 diameters. The disks were then cut in the dimensions of 10mm × 5mm × 1mm bilk samples by wire electrical discharge (EDM) machining. Nine substrate specimens (three from each alloy) surface were prepared by the metallographic method using a series of SiC grinding papers up to 2500 grit, followed by cloth polishing with 0.3 µm alumina suspension. In order to remove any contamination remaining on the surfaces, the specimens were ultrasonically cleaned by immersing them for 20 minutes in ethanol, acetone, and then deionized water.

Table 3.1: Nominal and actual chemical compositions (at %) of HEAs analyzed using EDX analysis

	TiTaHfNb		TiTaHfNbZr		TiTaHfMoZr	
	Nominal	Actual	Nominal	Actual	Nominal	Actual
Ti	50	52.69	20	21.72	20	21.99
Ta	16.7	16.04	20	18.69	20	20.08
Hf	16.7	15.78	20	18.74	20	19.68
Nb	16.7	15.49	20	18.97	0	0
Zr	0	0	20	21.88	20	19.95
Mo	0	0	0	0	20	18.30

The silver coatings were deposited on the HEA substrates and silicon wafers utilizing RF magnetron sputtering by Nanovak NVTS-400. Surface characteristics and biocompatibility experiments were performed on the HEA substrates coated with silver. The cross-sectional inspections were carried out on the silicon wafers coated by silver under the same conditions with HEA substrates in order to simplify the sample preparation. The silver target was firstly pre-sputtered by Ar plasma to remove the surface impurities. The deposition process was done at room temperature under Argon atmosphere with the base pressure of 1×10^{-4} Pa, and the constant flow of 10 standard cubic centimeters per minute (SCCM), and work Argon pressure of 2 Pa. The magnetron power was set at 100 W, and the deposition rate was approximately 3 Å/s. The three different thicknesses were adjusted by varying the deposition time from 20 minutes to 60 minutes.

The microstructures and elemental distribution of the samples surface both prior to and after the coating process. The cross-section of films was investigated by a field

emission scanning electron microscope (SEM, Zeiss, Ultra Plus) and energy-dispersive X-ray spectroscopy (EDX), respectively. The present phases of the substrates were characterized by an X-ray diffractometer (XRD, Bruker D8 Advance) with Cu Kα radiation ranging from 5º to 90º. A grazing incidence X-ray diffraction (GIXRD) was utilized for the deposited films ranging from 20º to 80º with a 1º step size.

The coated samples were immersed in an simulated body fluid (SBF) solution with the composition shown in Table 3.2 [94] at Ph of 7.4 for 14 days inside polypropylene sealed tubes for the static immersion experiments. The solutions were kept at a constant temperature of 37º electronically controlled by a water bath to simulate the human body temperature and investigate its effect on corrosion. The required amount of solution for each sample was calculated according to the ratio of the volume-to-surface area of 20 ml/cm². After the immersion experiments, the metallic ion release from the coated samples was measured by an Agilent 7700x inductively coupled plasma mass spectrometer (ICP-MS). The compositions of oxide films forming on the coatings after immersion tests were measured by A Thermo-Scientific K-Alpha X-Ray Photoelectron Spectrometer (XPS).

Table 3.2: Order and amounts of ingredients for preparing 1000 ml of SBF

Order	Ingredients	Amount
1	NaCl	8.035 g
2	$NaHCO_3$	0.355 g
3	KCl	0.225 g
4	$K_2HPO_4.3H_2O$	0.231 g
5	$MgCl_2.6H_2O$	0.311 g
6	1.0_M-HCl	39 ml
7	$CaCl_2$	0.292 g
8	Na_2SO_4	0.072 g
9	Tris	6.118 g
10	1.0_M-HCl	0–5 ml

3.3 Results and discussion

3.3.1 Microstructural characterizations

The XRD patterns of TiTaHfNb, TiTaHfNbZr, and TiTaHfMoZr HEA substrates and their crystal plane indices and peaks information are presented in Figure *3.1* and Table *3.3*, respectively. Accordingly, all the HEAs consist of a single BCC phase, and the lattice parameters correspond to TiTaHfNb, TiTaHfNbZr, and TiTaHfMoZr, respectively. The XRD pattern of the silver coating measured by GIXRD because of their very thin thickness for more accuracy is provided in Figure *3.2*. The patterns were taken for all three coating thicknesses, indicating that the silver coating is an FCC phase with lattice parameters and peaks information given in Table 3.4.

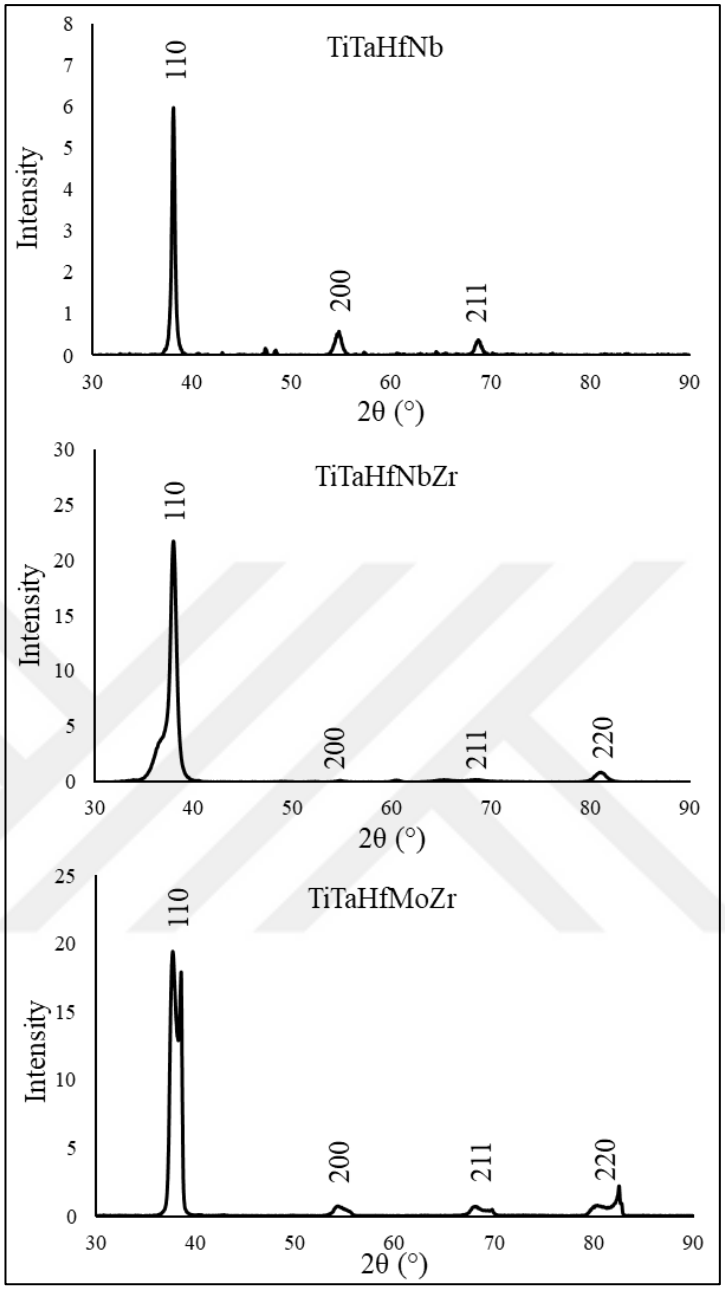

Figure 3.1: XRD results of as-cast (a) TiTaHfNb, (b) TiTaHfNbZr, and (c) TiTaHfMoZr HEAs.

Table 3.3: Summary of parameters extracted from XRD patterns of HEAs

Specimen	Peak number	2θ/ (°)	Lattice parameter (Å)
TiTaHfNb	1	38.12	3.33
	2	54.73	
	3	68.75	
TiTaHfNbZr	1	37.91	
	2	54.68	3.34
	3	81.02	
TiTaHfMoZr	1	37.70	
	2	38.54	3.36
	3	54.26	

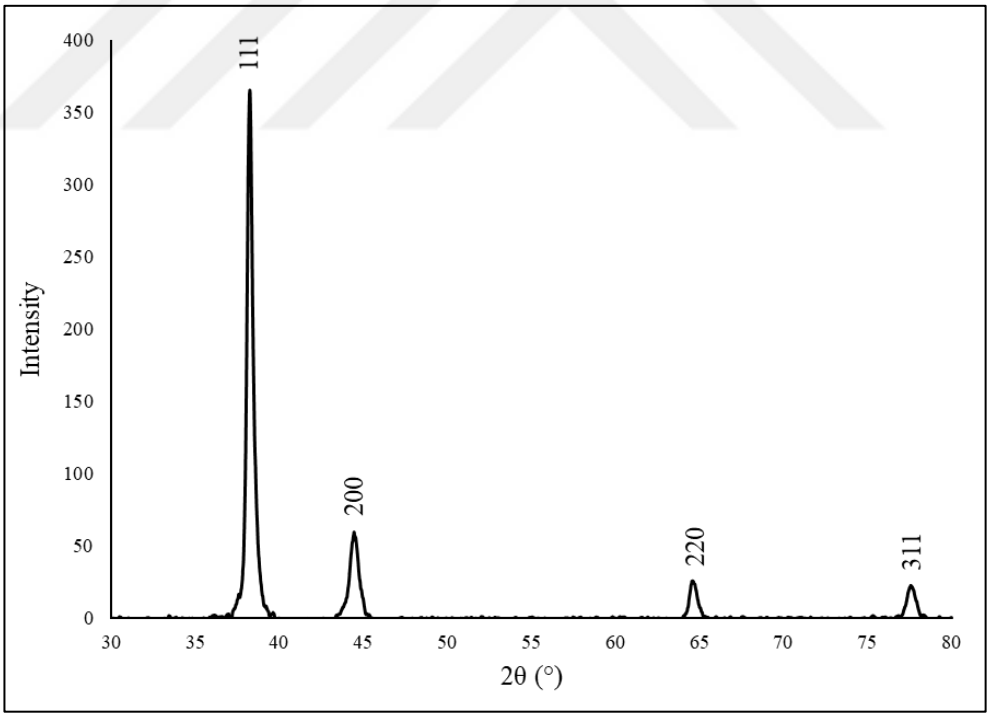

Figure 3.2: GIXRD result of silver- coated on HEA

Table 3.4: Summary of parameters extracted from GIXRD patterns of sliver coatings obtained at three deposition durations

Specimen	Peak number	2θ/ (°)	Lattice parameter (Å)
Silver 20 minutes coating	1	38.18	4.07
	2	42.68	
	3	64.61	
	4	77.47	
Silver 40 minutes coating	1	38.17	4.09
	2	42.72	
	3	64.23	
	4	73.17	
Silver 60 minutes coating	1	38.24	4.06
	2	44.44	
	3	64.58	
	4	77.58	

The surface morphology of the bulk HEAs is investigated by SEM analysis indicating the prepared specimens are composed of a single-phase and also the smooth surface of substrates prior to the coating process, as illustrated in Figure 3.3. Figure 3.4 shows the silver coatings at deposition durations of 10, 20, and 60 minutes revealing the homogenous coating on all the substrates. By increasing the deposition time while all the other parameters were kept constant, the thickness of the coating increased relatively linearly, as shown in Figure 3.5. The increasing of coating thickness might lead to enhancing the antibacterial performance since it leads to larger amounts of silver ion release. It has been reported that the antibacterial effect mainly depends on the total amount of silver released from the coating, which contributes to the antibacterial performance [93].

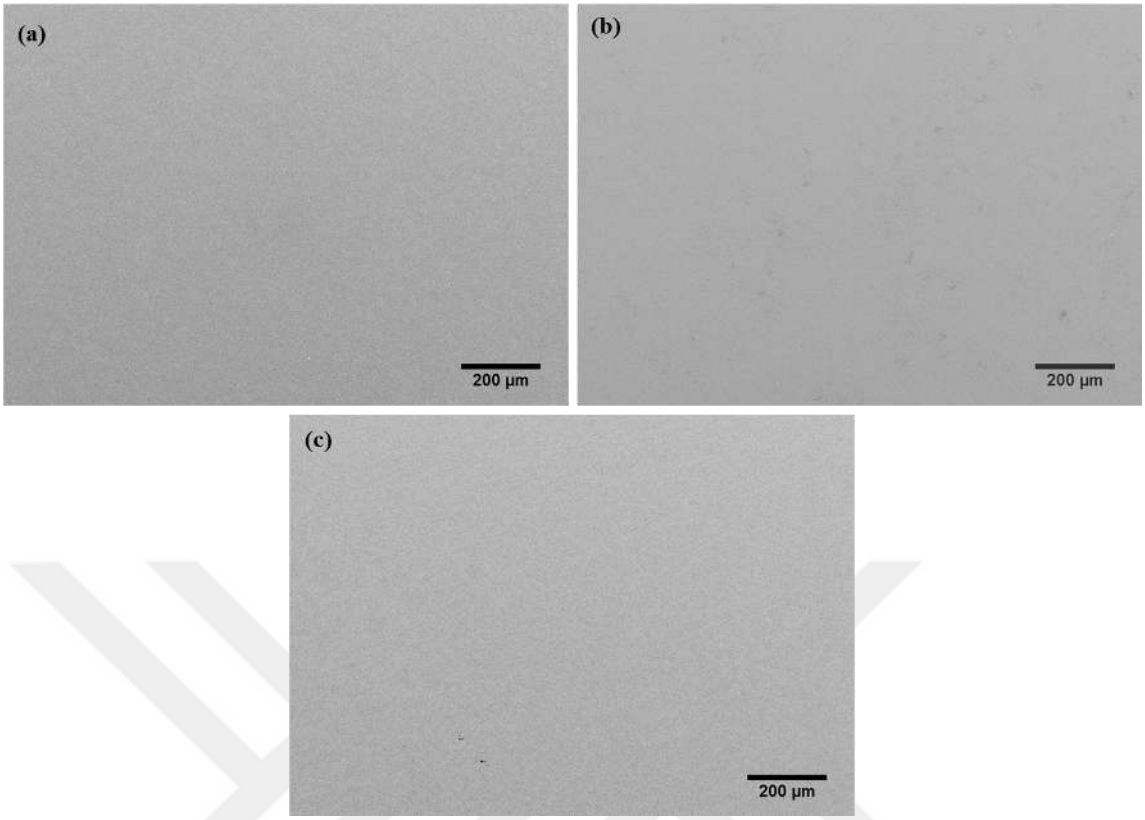

Figure 3.3: SEM images of substrates prior to coatings (a) TiTaHfNb (b) TiTaHfNbZr (c) TiTaHfMoZr

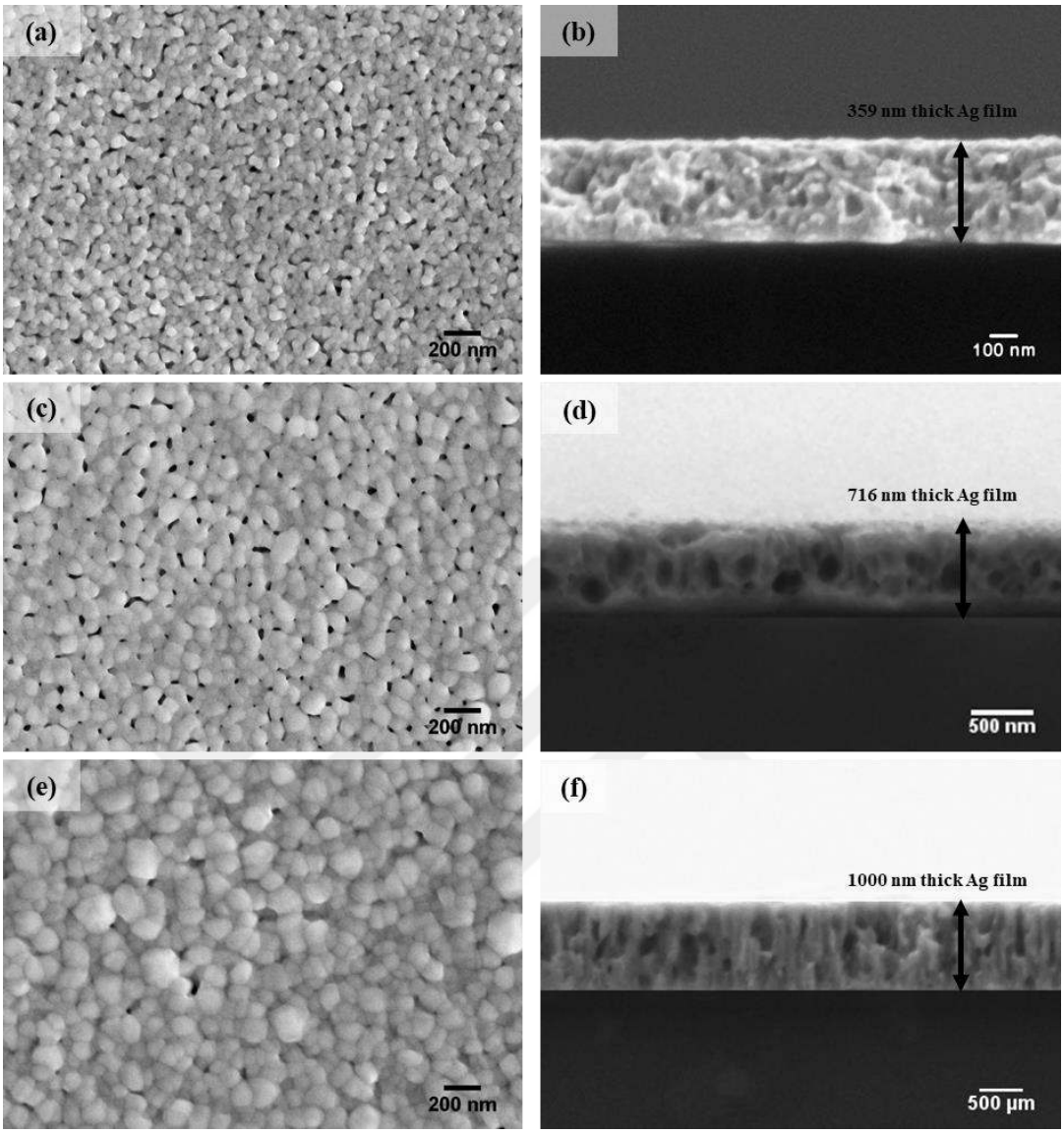

Figure 3.4: SEM images of silver films at deposition durations of: (a) 20 minutes on HEA substrate plane view (b) 20 minutes cross-sectional view on silicon (c) 40 minutes on HEA substrate plane view (c) 40 minutes cross-sectional view on silicon (d) 60 minutes on HEA substrate plane view (e) 60 minutes cross-sectional view on silicon

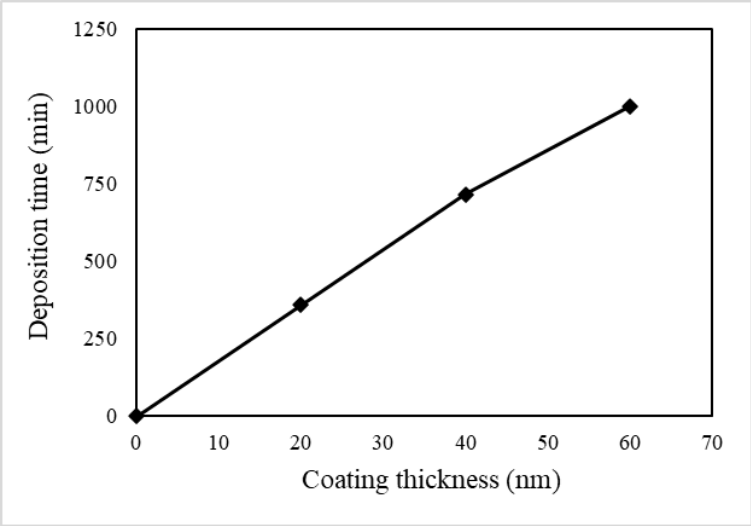

Figure 3.5: Silver thickness vs. deposition time obtained on HEA substrates

The SEM images reveal that the prolonged deposition time led to increasing the grain size significantly. It is known that by increasing the magnetron deposition duration, the silver particles aggregate more and become denser on the substrate. Thus, the collision probability between the sputtered silver particles and the deposited particles significantly increases which as a result contributes to a larger grain size [93]. Furthermore, it is also known that grain growth may occur when the coating grain size is smaller than the film thickness, which is also the case in this study. In such a case, grain growth happens, which is dominated by surface diffusion mass transport since there are no opposing terms such as grooving or curvature driven growth [95]. Another possible explanation of grain growth by increasing deposition duration might be due to the continuous accumulation of silver nanoparticles at longer deposition periods. This phenomenon can cause fewer nucleation sites available on the substrate, which will result in limiting the new smaller grains formation [96]. The accumulated silver particles might also be fused together and create larger crystalline grains. On the other hand, the longer deposition time resulted in more coverage of silver coatings on the substrates, which can lead to a larger release of Ag ions and thus improve the antibacterial activity.

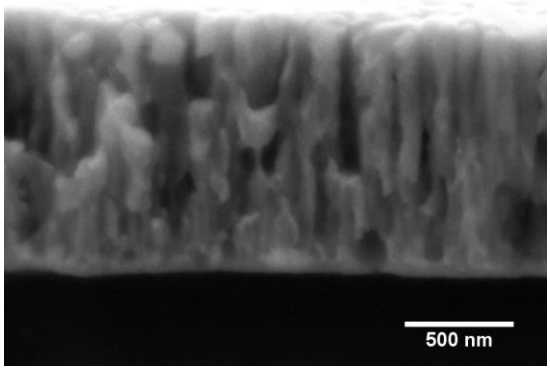

Figure 3.6: Cross-sectional view of silver coating on HEA at deposition time of 60 minutes

One of the common features of the metallic films is cauliflower-like grains [97] which are also observed in the coating of this study, as shown in Figure 3.4 and. These grain shapes can be caused by nodular growth, which is a common feature in thick coatings. Nodules grow within a columnar structure and appear to the surface as dome-shaped tops and form various overgrowths. These nodules can emerge as individuals or grow together and overlap and create complex aggregates, which leads to cauliflower-like structures. The columnar structure was observed in the coatings with 60 minutes deposition duration, as shown in Figure 3.6. It is reported that these nodules are dependent on the coating thickness and their height and width grows as the coating thickness increases. It is also shown that nodular growth is mainly associated with surface defects such as steps, ledges, and impurities rather than surface stresses [72].

3.3.2 Biocompatibility characterization

As seen in Figure 3.7, the SEM micrographs of TiTaHfNb samples with three different coatings, indicate a highly corroded surface following 14 days immersion in SBF. Figure 3.7 (a) and (b) shows that the silver coating was negatively affected by SBF through the thickness which caused cracks on the coating that may result in pitting corrosion in long term application. It can also be seen in Figure 3.4 (c) to (f) that by increasing the coating thickness the cracks and holes of the coating created by immersion reduced. It has been reported that the silver coating thickness was the most important factor in corrosion resistance for both silver and substrate such that the thinner coatings results in less corrosion resistance [98]. On the other hand, the SBF solution can be inContact with the

HEAs substrates through the cracks of the silver coatings that can cause substrates corrosion as well. Several studies demonstrated that chloride ion present in SBF have significant effect on corrosion of metals including HEAs [99]. HEAs are susceptive to pitting corrosion in chloride environments due to their lower pitting potential and narrower range of potentials in passive region.

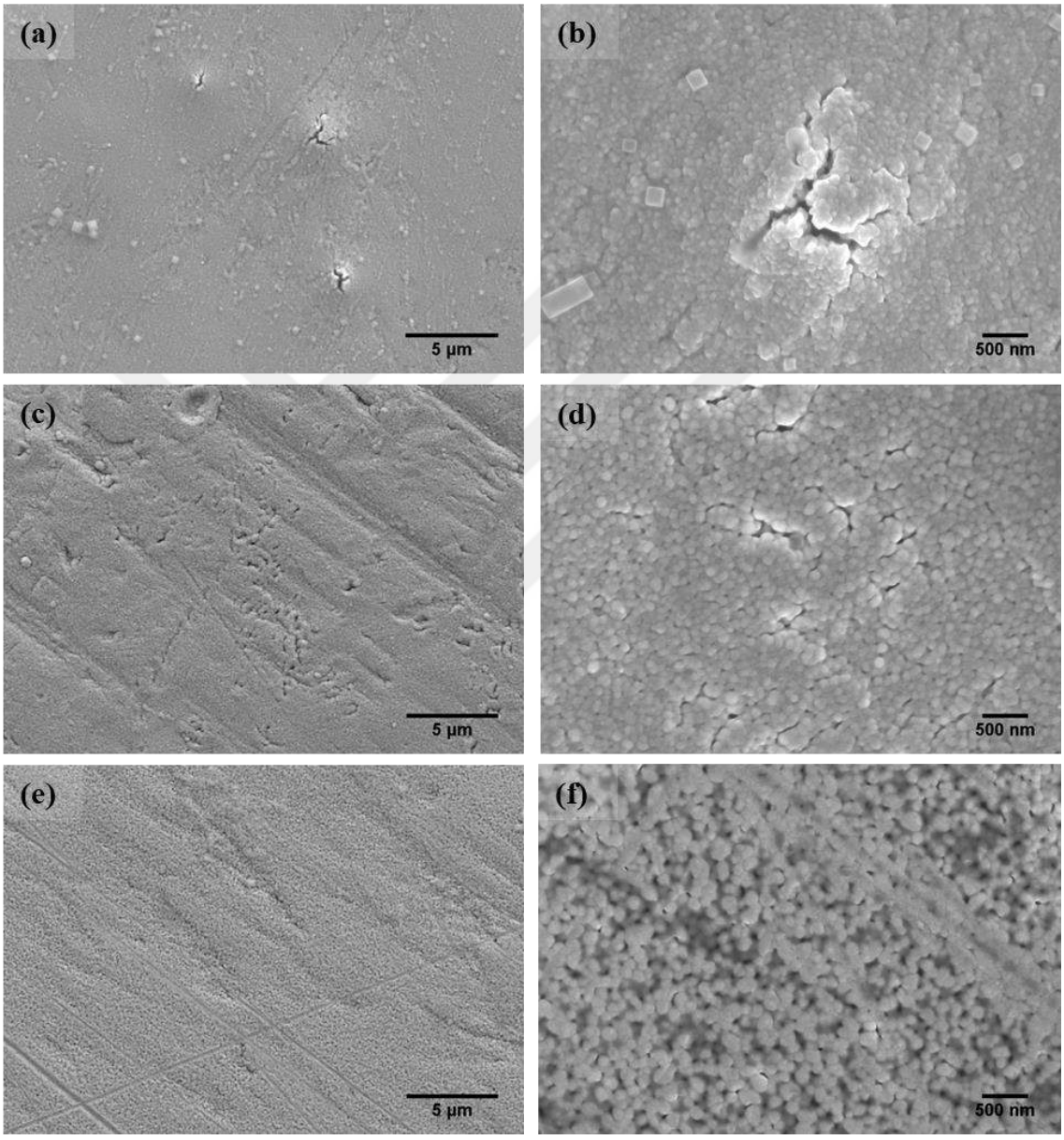

Figure 3.7: SEM micrographs of the TiTaHfNb coated surfaces by Ag following immersion for 14 days in SBF (a), (b): 20 minutes coating, (c), (d): 40 minutes coating, (e), (f): 60 minutes coating

As shown in *Figure 3.8*, SBF contains very similar amount of ion concentration for all three HEA substrates after immersion for all different coating thicknesses indicating that

coating thickness does not have a significant effect on substrates ion release. It can also be seen that the release of Ag ions increased by increasing the deposition duration which contributes to higher thickness of coatings and thus higher amount of silver on substrates. As illustrated in *Figure 3.8* (c), TiTaHfMoZr showed significantly higher amount of ion release into SBF which can be attributed to the presence of Mo in the alloy and nonhomogeneous distribution of components.

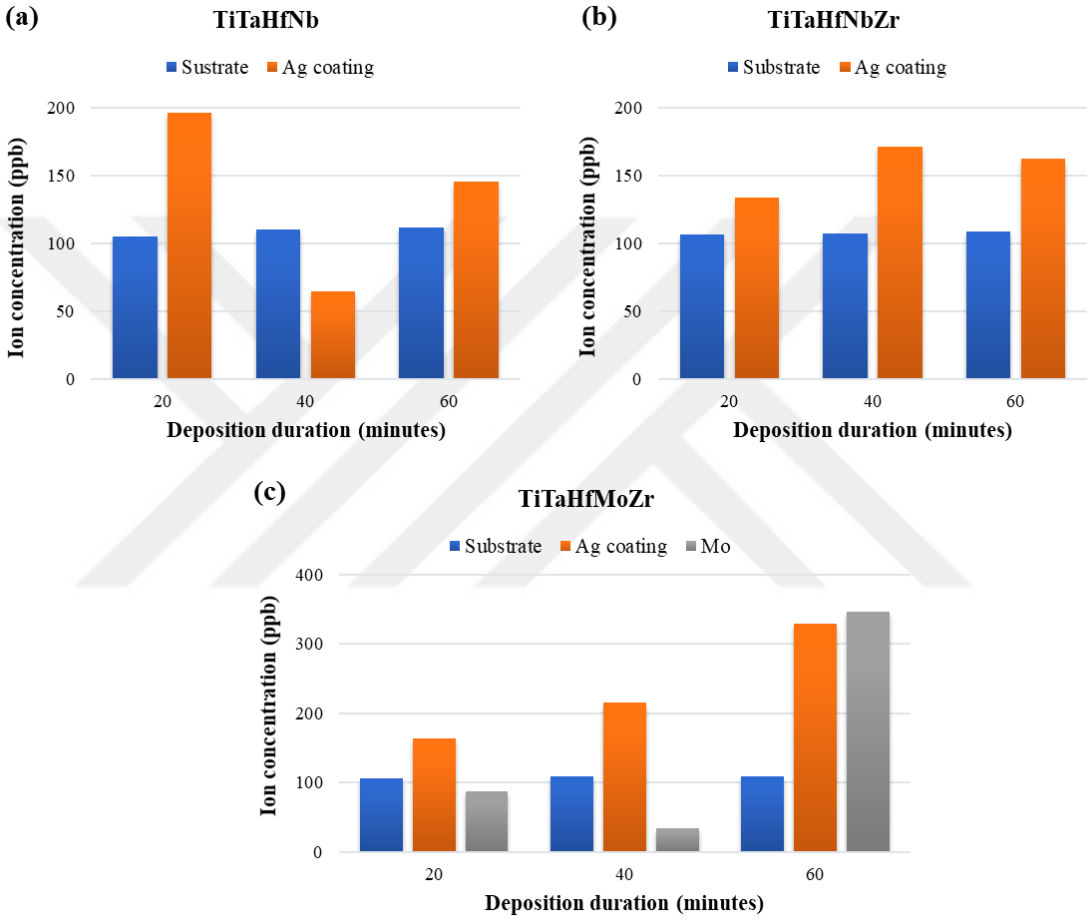

Figure 3.8: Total ion concentrations of Ag coatings and (a) Ti, Ta and Nb released from TiTaHfNb; (b) Ti, Ta, Nb and Zr released from TiTaHfNbZr; and (c) Ti, Ta, Nb, Mo and Zr released from TiTaHfMoZr. From immersion in SBF for 14 days.

The back scattered electron (BSE) images of TiTaHfMoZr presented in Figure 3.9 shows a dendritic structure that coexistence of two regions illustrated in black and white colors. The dendritic structure may be formed during solidification process due to inhomogeneous distribution of elements [16]. As illustrated by EDX analysis in Figure 3.9 (b) and (d), the dendrites observed within darker region consist of heavier elements and are Ta-rich with higher melting point that leads to their earlier crystallization where

inter-dendrite area is Zr-rich [100]. Figure 3.8 (c), indicates higher ion release of the HEA containing Mo than the other two substrates which can be due to the preferred corrosion of inter-dendrite phase over the dendrites because of their compositional difference. In addition, the significant higher amount of ion release from TiTaHfMoZr can be also attributed to the replacement of Nb by Mo, since Nb performs as a stabilizer which prohibits the release of ions [101, 102].

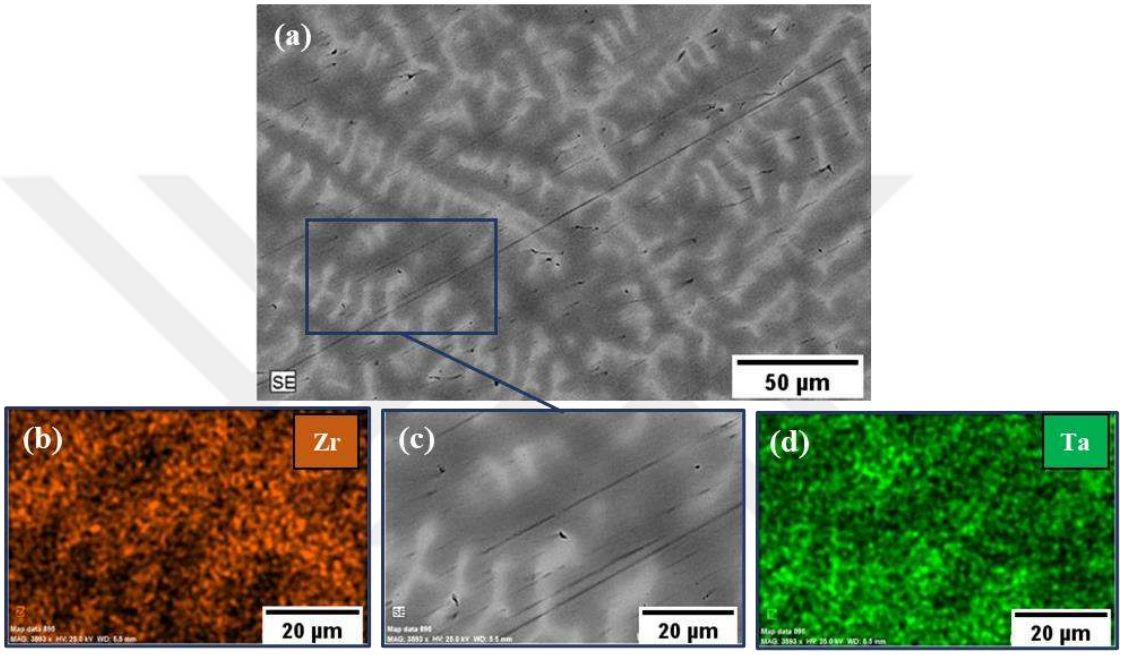

Figure 3.9: EDX analysis results of the as-received TiTaHfMoZr sample: (a) and (c) BSE image of the nonhomogeneous region. (b) and (d) Red regions represent Zr-rich areas and green regions represent Ta-rich areas.

In order to investigate the ion release more thoroughly and clarify the formation of passive oxide layers on the coatings after the immersion experiments, an XPS analysis was performed. Examination of the XPS results on the coated samples following 14 days of immersion in SBF (Figure *3.10*) revealed that only silver and silver oxides exist on the surface until 600 s etching time. Consequently, one can conclude that all the coatings covered the substrates completely and no oxides of substrates were observed.

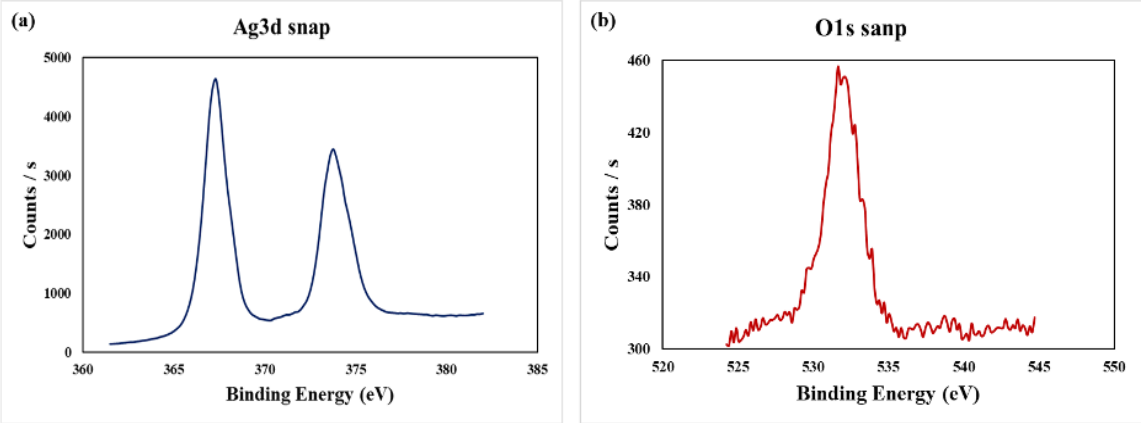

Figure 3.10: XPS depth profiles of silver coatings with 60 minutes deposition duration following 14 days immersion in SBF (a) Silver peaks after 600 s etch time, (b) Oxygen peak with no etching

The 3D AFM surface topography images of the three different silver coatings are shown in *Figure 3.11*. The roughness measurements for the coatings with 20, 40, and 60 minutes deposition duration are 5.75 nm, 8.20 nm, and 46.3 nm respectively. As it is illustrated, by increasing the deposition time the coatings roughness values increase dramatically. It has been reported that for thin films, by increasing the surface roughness the coefficient of friction and wear rate generally decreases [97] which can enhance the antibacterial properties since the coating can remain on the substrate for longer durations.

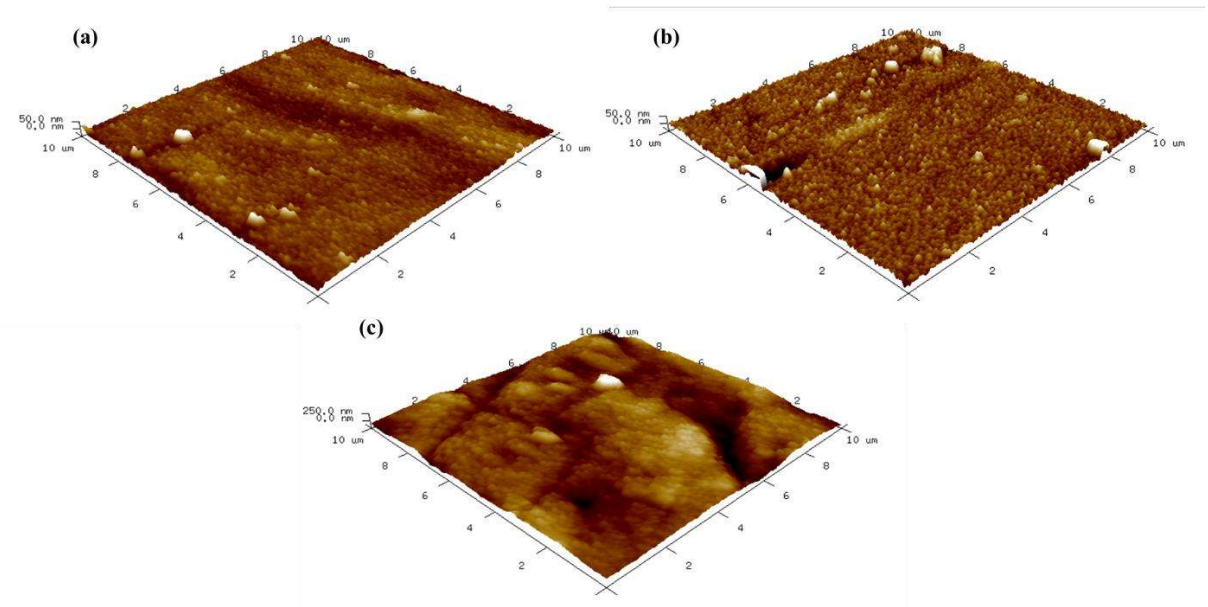

Figure 3.11: The 3D AFM images of silver coatings: (a) 20 minutes deposition duration, (b) 40 minutes deposition duration, (c) 60 minutes deposition duration.

Chapter 4:
CONCLUSION

In this study, silver coatings were deposited on three different biocompatible high entropy alloys in order to introduce antibacterial properties to the substrates. The coatings were deposited at three different thicknesses by adjusting the PVD device parameters. It can be seen from the SEM images that by increasing the deposition duration, a significant grain growth occurred. The grain growth phenomenon might have happened due to various reasons, such as increasing the collision of silver particles and accumulation of them by increasing the deposition time. Furthermore, the coated specimen was immersed in an SBF solution to evaluate the ion release of substrates and their coating. The ion release measurements revealed that the Ag ion release increased by increasing the deposition time and thus silver thickness as expected. The higher amount of Ag ions enhances the antibacterial effect of the alloy. It was also seen that the ion release of the HEA substrates did not affect by coating thickness, and they all presented relatively same amount of ion release. TiTaHfMoZr exhibited the highest amount of ion release which were mainly Mo ions that may be related to the dendritic structure and inhomogeneous microstructure of the alloy and thus more susceptive to pitting corrosion. The XPS results of coatings after immersion tests revealed that all of the coatings with different thicknesses covered the substrates completely and no peaks from them was observed. The AFM measurements on the coatings showed that by increasing the deposition duration and the coating thickness, the roughness of the surfaces are increasing which might decrease the wear rate.

Bibliography

1. Gao, M.C., et al., *High-entropy alloys.* Cham: Springer International Publishing, 2016.
2. Huang, P.-K., et al., *Multi-Principal-Element Alloys with Improved Oxidation and Wear Resistance for Thermal Spray Coating.* Advanced Engineering Materials, 2004. **6**(1-2): p. 74-78.
3. Yeh, J.W., et al., *Nanostructured high-entropy alloys with multiple principal elements: novel alloy design concepts and outcomes.* Advanced Engineering Materials, 2004. **6**(5): p. 299-303.
4. Cantor, B., et al., *Microstructural development in equiatomic multicomponent alloys.* Materials Science and Engineering: A, 2004. **375**: p. 213-218.
5. Chen, T.K., et al., *Nanostructured nitride films of multi-element high-entropy alloys by reactive DC sputtering.* Surface and Coatings Technology, 2004. **188-189**: p. 193-200.
6. Hsu, C.-Y., et al., *Wear resistance and high-temperature compression strength of Fcc CuCoNiCrAl0.5Fe alloy with boron addition.* Metallurgical and Materials Transactions A, 2004. **35**(5): p. 1465-1469.
7. Yeh, J.-W., et al., *Formation of simple crystal structures in Cu-Co-Ni-Cr-Al-Fe-Ti-V alloys with multiprincipal metallic elements.* Metallurgical and Materials Transactions A, 2004. **35**(8): p. 2533-2536.
8. George, E.P., D. Raabe, and R.O. Ritchie, *High-entropy alloys.* Nature Reviews Materials, 2019. **4**(8): p. 515-534.
9. RA, S., *Thermodynamics of solids.* John Wiley and Sons, 1972) p, 1972. **178**.
10. Jien-Wei, Y., *Recent progress in high entropy alloys.* Ann. Chim. Sci. Mat, 2006. **31**(6): p. 633-648.
11. Eißmann, N., et al., *High-entropy alloy CoCrFeMnNi produced by powder metallurgy.* Powder Metallurgy, 2017. **60**(3): p. 184-197.
12. Tsai, K.Y., M.H. Tsai, and J.W. Yeh, *Sluggish diffusion in Co–Cr–Fe–Mn–Ni high-entropy alloys.* Acta Materialia, 2013. **61**(13): p. 4887-4897.
13. Zhou, Y., et al., *Solid solution alloys of Al Co Cr Fe Ni Ti x with excellent room-temperature mechanical properties.* Applied physics letters, 2007. **90**(18): p. 181904.
14. Motallebzadeh, A., et al., *Microstructural, mechanical and electrochemical characterization of TiZrTaHfNb and Ti1.5ZrTa0.5Hf0.5Nb0.5 refractory high-entropy alloys for biomedical applications.* Intermetallics, 2019. **113**: p. 106572.
15. Zhang, Y., X. Yang, and P.K. Liaw, *Alloy Design and Properties Optimization of High-Entropy Alloys.* JOM, 2012. **64**(7): p. 830-838.
16. Gurel, S., et al., *Corrosion behavior of novel Titanium-based high entropy alloys designed for medical implants.* Materials Chemistry and Physics, 2020. **254**: p. 123377.
17. Tang, Z., et al., *Alloying and Processing Effects on the Aqueous Corrosion Behavior of High-Entropy Alloys.* Entropy, 2014. **16**(2): p. 895-911.
18. Qiu, Y., et al., *Corrosion characteristics of high entropy alloys.* Materials Science and Technology, 2015. **31**(10): p. 1235-1243.
19. Nong, Z.-S., et al., *Stability and structure prediction of cubic phase in as cast high entropy alloys.* Materials Science and Technology, 2014. **30**(3): p. 363-369.

20. Wu, Y., et al., *A refractory Hf25Nb25Ti25Zr25 high-entropy alloy with excellent structural stability and tensile properties.* Materials Letters, 2014. **130**: p. 277-280.
21. Niinomi, M., *Recent metallic materials for biomedical applications.* Metallurgical and Materials Transactions A, 2002. **33**(3): p. 477.
22. Aksoy, C., D. Canadinc, and M. Yagci, *Assessment of Ni ion release from TiTaHfNbZr high entropy alloy coated NiTi shape memory substrates in artificial saliva and gastric fluid.* Materials Chemistry and Physics, 2019. **236**: p. 121802.
23. Okazaki, Y. and E. Gotoh, *Comparison of metal release from various metallic biomaterials in vitro.* Biomaterials, 2005. **26**(1): p. 11-21.
24. Niinomi, M., *Development of high biocompatible titanium alloys.* Kino Zairyo(Function and Materials)(Japan), 2000. **20**(3): p. 36-44.
25. Ma, N., et al., *Research progress of titanium-based high entropy alloy: methods, properties, and applications.* Frontiers in Bioengineering and Biotechnology, 2020. **8**: p. 1303.
26. Zhang, Y., et al., *Microstructures and properties of high-entropy alloys.* Progress in Materials Science, 2014. **61**: p. 1-93.
27. Todai, M., et al., *Novel TiNbTaZrMo high-entropy alloys for metallic biomaterials.* Scripta Materialia, 2017. **129**: p. 65-68.
28. Nagase, T., et al., *Microstructure of equiatomic and non-equiatomic Ti-Nb-Ta-Zr-Mo high-entropy alloys for metallic biomaterials.* Journal of Alloys and Compounds, 2018. **753**: p. 412-421.
29. Hori, T., et al., *Development of non-equiatomic Ti-Nb-Ta-Zr-Mo high-entropy alloys for metallic biomaterials.* Scripta Materialia, 2019. **172**: p. 83-87.
30. Wang, S.-P. and J. Xu, *TiZrNbTaMo high-entropy alloy designed for orthopedic implants: As-cast microstructure and mechanical properties.* Materials Science and Engineering: C, 2017. **73**: p. 80-89.
31. Akmal, M., et al., *Systematic Study of (MoTa) xNbTiZr Medium-and High-Entropy Alloys for Biomedical Implants-In Vivo Biocompatibility Examination.* Journal of Materials Science & Technology, 2021. **78**: p. 183-191.
32. Matsuno, H., et al., *Biocompatibility and osteogenesis of refractory metal implants, titanium, hafnium, niobium, tantalum and rhenium.* Biomaterials, 2001. **22**(11): p. 1253-1262.
33. Yuan, Y., et al., *Formation, structure and properties of biocompatible TiZrHfNbTa high-entropy alloys.* Materials Research Letters, 2019. **7**(6): p. 225-231.
34. Nagase, T., et al., *Design and fabrication of Ti–Zr-Hf-Cr-Mo and Ti–Zr-Hf-Co-Cr-Mo high-entropy alloys as metallic biomaterials.* Materials Science and Engineering: C, 2020. **107**: p. 110322.
35. Zhang, C., et al., *Computational thermodynamics aided high-entropy alloy design.* Jom, 2012. **64**(7): p. 839-845.
36. Saal, J.E., et al., *Equilibrium high entropy alloy phase stability from experiments and thermodynamic modeling.* Scripta Materialia, 2018. **146**: p. 5-8.
37. Lederer, Y., et al., *The search for high entropy alloys: a high-throughput ab-initio approach.* Acta Materialia, 2018. **159**: p. 364-383.
38. Sanchez, J.M., et al., *Phase prediction, microstructure and high hardness of novel light-weight high entropy alloys.* Journal of Materials Research and Technology, 2019. **8**(1): p. 795-803.

39. Senkov, O., et al., *Accelerated exploration of multi-principal element alloys for structural applications.* Calphad, 2015. **50**: p. 32-48.
40. Li, Y., et al., *New developments of Ti-based alloys for biomedical applications.* Materials, 2014. **7**(3): p. 1709-1800.
41. Ramprasad, R., et al., *Machine learning in materials informatics: recent applications and prospects.* npj Computational Materials, 2017. **3**(1): p. 1-13.
42. Meredig, B., et al., *Combinatorial screening for new materials in unconstrained composition space with machine learning.* Physical Review B, 2014. **89**(9): p. 094104.
43. Tepla, T., et al., *Alloys selection based on the supervised learning technique for design of biocompatible medical materials.* Archives of Materials Science and Engineering, 2018. **93**(1): p. 32-40.
44. Diao, Y., L. Yan, and K. Gao, *Improvement of the machine learning-based corrosion rate prediction model through the optimization of input features.* Materials & Design, 2021. **198**: p. 109326.
45. Wen, C., et al., *Machine learning assisted design of high entropy alloys with desired property.* Acta Materialia, 2019. **170**: p. 109-117.
46. Huang, W., P. Martin, and H.L. Zhuang, *Machine-learning phase prediction of high-entropy alloys.* Acta Materialia, 2019. **169**: p. 225-236.
47. Zhou, Z., et al., *Machine learning guided appraisal and exploration of phase design for high entropy alloys.* npj Computational Materials, 2019. **5**(1): p. 1-9.
48. Machaka, R., *Machine learning-based prediction of phases in high-entropy alloys.* Computational Materials Science, 2021. **188**: p. 110244.
49. Islam, N., W. Huang, and H.L. Zhuang, *Machine learning for phase selection in multi-principal element alloys.* Computational Materials Science, 2018. **150**: p. 230-235.
50. Alpaydin, E., *Introduction to machine learning*. 2020: MIT press.
51. Butler, K.T., et al., *Machine learning for molecular and materials science.* Nature, 2018. **559**(7715): p. 547-555.
52. Cios, K.J., et al., *Unsupervised Learning: Clustering*, in *Data Mining: A Knowledge Discovery Approach*, K.J. Cios, et al., Editors. 2007, Springer US: Boston, MA. p. 257-288.
53. Murtagh, F. and P. Contreras, *Algorithms for hierarchical clustering: an overview.* Wiley Interdisciplinary Reviews: Data Mining and Knowledge Discovery, 2012. **2**(1): p. 86-97.
54. Blashfield, R.K. and M.S. Aldenderfer, *The literature on cluster analysis.* Multivariate behavioral research, 1978. **13**(3): p. 271-295.
55. Müllner, D., *Modern hierarchical, agglomerative clustering algorithms.* arXiv preprint arXiv:1109.2378, 2011.
56. Virtanen, P., et al., *SciPy 1.0: fundamental algorithms for scientific computing in Python.* Nature methods, 2020. **17**(3): p. 261-272.
57. Bar-Joseph, Z., D.K. Gifford, and T.S. Jaakkola, *Fast optimal leaf ordering for hierarchical clustering.* Bioinformatics, 2001. **17**(suppl_1): p. S22-S29.
58. Gower, J.C. and G.J. Ross, *Minimum spanning trees and single linkage cluster analysis.* Journal of the Royal Statistical Society: Series C (Applied Statistics), 1969. **18**(1): p. 54-64.
59. Wenzlick, M., et al., *Data science techniques, assumptions, and challenges in alloy clustering and property prediction.* Journal of Materials Engineering and Performance, 2021. **30**(2): p. 823-838.

60. Garikapati, P., et al., *A Cluster-Profile Comparative Study on Machining AlSi 7/63% of SiC Hybrid Composite Using Agglomerative Hierarchical Clustering and K-Means.* Silicon, 2021. **13**: p. 961-972.
61. Castro, D., et al., *An Overview of High-Entropy Alloys as Biomaterials.* Metals, 2021. **11**(4): p. 648.
62. Geanta, V., et al., *High entropy alloys for medical applications.* Engineering Steels and High Entropy-Alloys, 2019: p. 1-17.
63. Chen, Q. and G.A. Thouas, *Metallic implant biomaterials.* Materials Science and Engineering: R: Reports, 2015. **87**: p. 1-57.
64. Zhao, L., et al., *Antibacterial coatings on titanium implants.* Journal of Biomedical Materials Research Part B: Applied Biomaterials, 2009. **91**(1): p. 470-480.
65. Lansdown, A.B., *Silver in health care: antimicrobial effects and safety in use.* Biofunctional textiles and the skin, 2006. **33**: p. 17-34.
66. Berger, T., et al., *Electrically generated silver ions: quantitative effects on bacterial and mammalian cells.* Antimicrobial agents and chemotherapy, 1976. **9**(2): p. 357-358.
67. Melaiye, A. and W.J. Youngs, *Silver and its application as an antimicrobial agent*. 2005, Taylor & Francis.
68. Kedziora, A., et al., *Synthesis and antibacterial activity of novel titanium dioxide doped with silver.* Journal of sol-gel science and technology, 2012. **62**(1): p. 79-86.
69. Ewald, A., et al., *Antimicrobial titanium/silver PVD coatings on titanium.* BioMedical Engineering OnLine, 2006. **5**(1): p. 22.
70. Mrkvica, I., et al., *Properties and comparison of PVD coatings.* 2016.
71. Eckertova, L., *Physics of thin films*. 2012: Springer Science & Business Media.
72. Spalvins, T. and W. Brainard, *Nodular growth in thick-sputtered metallic coatings.* Journal of Vacuum Science and Technology, 1974. **11**(6): p. 1186-1192.
73. Charton, C. and M. Fahland, *Growth of Ag films on PET deposited by magnetron sputtering.* Vacuum, 2002. **68**(1): p. 65-73.
74. Maréchal, N., E. Quesnel, and Y. Pauleau, *Characterization of silver films deposited by radio frequency magnetron sputtering.* Journal of Vacuum Science & Technology A, 1994. **12**(3): p. 707-713.
75. Cardarelli, F., *Materials handbook*. 2018: Springer.
76. KÖSter, W. and H. Franz, *POISSON'S RATIO FOR METALS AND ALLOYS.* Metallurgical Reviews, 1961. **6**(1): p. 1-56.
77. Yamamoto, A., R. Honma, and M. Sumita, *Cytotoxicity evaluation of 43 metal salts using murine fibroblasts and osteoblastic cells.* Journal of Biomedical Materials Research, 1998. **39**(2): p. 331-340.
78. Mizutani, U., *Hume-Rothery rules for structurally complex alloy phases.* Mrs Bulletin, 2012. **37**(2): p. 169-169.
79. Clementi, E., D.L. Raimondi, and W.P. Reinhardt, *Atomic Screening Constants from SCF Functions. II. Atoms with 37 to 86 Electrons.* The Journal of Chemical Physics, 1967. **47**(4): p. 1300-1307.
80. Guo, S. and C.T. Liu, *Phase stability in high entropy alloys: Formation of solid-solution phase or amorphous phase.* Progress in Natural Science: Materials International, 2011. **21**(6): p. 433-446.

81. Vitos, L., et al., *The surface energy of metals.* Surface Science, 1998. **411**(1): p. 186-202.
82. Pedregosa, F., et al., *Scikit-learn: Machine learning in Python.* the Journal of machine Learning research, 2011. **12**: p. 2825-2830.
83. Jha, R., et al., *Magnetic Alloys Design Using Multi-objective Optimization*, in *Properties and Characterization of Modern Materials*, A. Öchsner and H. Altenbach, Editors. 2017, Springer Singapore: Singapore. p. 261-284.
84. Song, X., et al., *Improvement in fatigue strength while keeping low Young's modulus of a β-type titanium alloy through yttrium oxide dispersion.* Materials Science and Engineering: C, 2012. **32**(3): p. 542-549.
85. Weng, W., et al., *Impact of the rare earth elements scandium and yttrium on beta-type Ti-24Nb-38Zr-2Mo-base alloys for orthopedic applications.* Materialia, 2020. **9**: p. 100586.
86. Xu, P., et al., *Impacts of yttrium on microstructure and tensile properties of biomedical β Ti-Nb-Zr fabricated by metal injection molding.* Materials Science and Engineering: A, 2020. **792**: p. 139816.
87. Tan, P.-N., M. Steinbach, and V. Kumar, *Introduction to data mining, Pearson education.* Inc., New Delhi, 2006.
88. Palacio-Niño, J.-O. and F. Berzal, *Evaluation metrics for unsupervised learning algorithms.* arXiv preprint arXiv:1905.05667, 2019.
89. Caliński, T. and J. Harabasz, *A dendrite method for cluster analysis.* Communications in Statistics-theory and Methods, 1974. **3**(1): p. 1-27.
90. Koev, K., et al. *Antibacterial silver nanolayers for coatings on surgical and microsurgical instruments*. in *Journal of Physics: Conference Series*. 2020. IOP Publishing.
91. Liedberg, H. and T. Lundeberg, *Silver alloy coated catheters reduce catheter-associated bacteriuria.* British journal of urology, 1990. **65**(4): p. 379-381.
92. Marechal, N., E.a. Quesnel, and Y. Pauleau, *Silver thin films deposited by magnetron sputtering.* Thin solid films, 1994. **241**(1-2): p. 34-38.
93. Wang, H.B., et al., *Sputter deposition of nanostructured antibacterial silver on polypropylene non-wovens.* Surface Engineering, 2008. **24**(1): p. 70-74.
94. Kokubo, T. and H. Takadama, *How useful is SBF in predicting in vivo bone bioactivity?* Biomaterials, 2006. **27**(15): p. 2907-2915.
95. Dannenberg, R., et al., *TEM annealing study of normal grain growth in silver thin films.* Thin Solid Films, 2000. **379**(1): p. 133-138.
96. Jamuna-Thevi, K., et al., *Quantification of silver ion release, in vitro cytotoxicity and antibacterial properties of nanostuctured Ag doped TiO2 coatings on stainless steel deposited by RF magnetron sputtering.* Vacuum, 2011. **86**(3): p. 235-241.
97. Tüten, N., et al., *Microstructure and tribological properties of TiTaHfNbZr high entropy alloy coatings deposited on Ti6Al4V substrates.* Intermetallics, 2019. **105**: p. 99-106.
98. Imrell, T. *The importance of the thickness of silver coating in the corrosion behaviour of copper contacts*. in *Electrical Contacts-1991 Proceedings of the Thirty-Seventh IEEE HOLM Conference on Electrical Contacts*. 1991. IEEE.
99. Chen, Y.Y., et al., *Microstructure and electrochemical properties of high entropy alloys—a comparison with type-304 stainless steel.* Corrosion Science, 2005. **47**(9): p. 2257-2279.

100. Tseng, K.-K., et al., *Effects of Mo, Nb, Ta, Ti, and Zr on Mechanical Properties of Equiatomic Hf-Mo-Nb-Ta-Ti-Zr Alloys.* Entropy, 2019. **21**(1): p. 15.
101. Ghiban, B., et al. *Corrosion behaviour in human stimulation media of a high entropy titan-based alloy*. in *IOP Conference Series: Materials Science and Engineering*. 2018. IOP Publishing.
102. Niendorf, T., et al., *Microstructure–mechanical property relationships in ultrafine-grained NbZr.* Acta Materialia, 2007. **55**(19): p. 6596-6605.

Appendix A: Dataset for development of ML models

Elements	Density (kg/m3)	Surface Energy (J/m2)	Atomic Radii (A)	Melting point C	Pauling electronegativity
Rb	1.532	0.104	2.65	39.3	0.82
Cs	1.873	0.082	2.98	28.4	0.79
Be	1.847	1.834	1.12	1282.9	1.57
Sr	2.45	0.428	2.19	768.9	0.95
Ba	3.594	0.376	2.53	728.9	0.89
Y	4.496	1.506	2.12	1521.9	1.22
Ti	4.54	2.632	1.76	1668	1.54
Zr	6.506	2.26	2.06	1854.7	1.33
Hf	13.31	2.472	2.08	2229.9	1.3
V	6.16	3.285	1.71	1886.9	1.63
Nb	8.57	2.685	1.98	2467.9	1.6
Ta	16.65	3.084	2	2995.9	1.5
Cr	7.19	3.505	1.66	1856.9	1.66
Mo	10.22	3.454	1.9	2621.8	2.16
W	19.3	4.005	1.93	3413.8	2.36
Mn	7.44	3.1	1.61	1243.9	1.55
Fe	7.874	2.43	1.56	1534.9	1.83
Ru	12.37	3.928	1.78	2336.9	2.2
Co	8.9	2.595	1.52	1454.9	1.88
Rh	12.41	2.472	1.73	1963.9	2.28
Ir	22.65	2.971	1.8	2409.9	2.2
Ni	8.902	2.011	1.49	1452.9	1.91
Pd	12.02	1.92	1.69	554.9	2.2
Cu	8.96	1.952	1.45	1084.6	1.9
Ag	10.5	1.172	1.65	961.78	1.93
Zn	7.133	0.989	1.42	419.52	1.65
Cd	8.65	0.593	1.61	321	1.69
Al	2.699	1.199	1.18	660.32	1.61

In	7.31	0.488	1.56	156.59	1.78
Sn	7.298	0.611	1.45	231.93	1.96
Sb	6.696	0.608	1.33	630.7	2.05
Bi	9.747	0.537	1.43	271.4	2.02

No. of valance e	Young's Modulus (GPa)	Poisson's ratio	IC50_L929	IC50_MC3T3
1	2.35	0.35	1100	3520
1	1.69	0.295	3530	1320
2	318	0.075	94.2	2.28
2	15.7	0.28	11500	1080
2	12.8	0.28	2110	1260
3	63.5	0.27	254	142
4	120.2	0.36	1090	871
4	97.1	0.33	1640	2830
4	141	0.26	1160	933
5	127.6	0.37	2.82	2.25
5	104.9	0.39	3630	1470
5	185.7	0.35	1880	2060
6	279	0.21	743	12.7
6	324.8	0.3	1190	3520
6	411	0.3	622	320
7	191	0.24	45.9	38.1
8	208.2	0.29	5420	328
8	432	0.25	5850	999
9	243	0.29	81.2	11.2
9	379	0.26	407	21.4
9	528	0.26	151	12
10	199.5	0.31	106	52.2
10	121	0.39	174	558
11	129.8	0.343	274	34
11	82.7	0.37	4.25	2.77

12	104.5	0.25	92.8	90
12	62.6	0.29	2.51	1.36
3	70.2	0.345	4180	2920
3	10.6	0.45	145	2.03
4	49.9	0.33	141	25
5	54.7	0.25	16.8	2.49
5	34	0.33	764	12